UCLA
School
of
Engineering
and
Applied
Science

UCLA-ENG-88-28

HEAT PIPE DYNAMIC BEHAVIOR

F. Issacci, G.L. Roche, D.B. Klein and I. Catton
Mechanical, Aerospace and Nuclear Engineering Department
University of California
Los Angeles, CA   90024

Heat Pipe Dynamic Behavior

by

F. Issacci, G. L. Roche, D. B. Klein and I. Catton

Mechanical, Aerospace and Nuclear Engineering Department

University of California

Los Angeles

September 1988

CONTENTS

LIST OF FIGURES

NOMENCLATURE

A area (m^2)

A_w wick cross-sectional area of annulus (m^2)

b square channel width

c speed of sound based on stagnation temperature (m/s)

c_p specific heat at constant pressure $(J/kg \cdot K)$

C concentration

C_t terminal velocity

C_w coefficient of wick porosity

d beam diameter (m)

D diameter (m)

f body force (N) (Ch. VII)

       friction factor

$\dot{F}_l$ liquid flow friction coefficient (s/m^4)

g gravity acceleration

h_{fg} latent heat of vaporization (J/kg)

h_1 coefficient for determining radial phase change velocity

k thermal conductivity $(W/m \cdot K)$

K wick permability

l test section width (m)

L overall heat pipe length (m)

m total mass (kg)

$\dot{m}$ mass flux (kg/s)

M mass (kg) (Ch. VII)

           molecular weight $(kg/kgmole)$

n refractive index

N molar refractivity

p pressure (Pa)

$\bar{p}$ space averaged pressure (Pa)

$\tilde{p}$ pressure deviation (Pa)

P pressure (Pa)

Pr Prandtl number

q heat flux (W/m^2)

Q heat transfer rate (W)

r cylindrical coordinate radial direction

           radius of curvature (m)

r_h hydraulic radius (m)

r_p particle radius (m)

R gas constant $(J/kg{\cdot}K)$

           radius (m) (Ch. VII)

R_g gas constant $(J/kg{\cdot}K)$

R_u universal gas constant, 8314 $J/kgmole{\cdot}K$

R_1, R_2 radii of curvature of a meniscus surface (m)

Re Reynolds number

S interference order

St Stokes number

t	time (s)
T	temperature (K)
u	velocity component in axial direction (m/s)
u^*	dimensionless velocity component in axial direction
U	perpendicular velocity component of particle
$\overline{U}$	bulk axial velocity (m/s)
U_s	shift velocity
v	radial (or vertical) velocity (m/s)
V	volume (m^3)
$\not{V}$	volume (m^3) (Ch. VII)
V_0	liquid phase change radial velocity (m/s)
w	velocity component in the azimuthal direction (m/s)
x	axial coordinate
x,y,z	Cartesian coordinates
α	thermal diffusivity (m^2/s)
γ	ratio of principle specific heats
δ	liquid layer thickness (m)
δ_t	time step size (s)
Δp	pressure drop
Δz	fringe spacing
ε	wick porosity
λ	wavelength (m)
μ	dynamic viscosity $(kg/m{\cdot}s)$

v	kinematic viscosity (m^2/s)
v_D	Doppler frequency
v_s	frequency shift
ρ	density (kg/m^3)
σ	surface tension (N/m)
	Stefan-Boltzmann constant, $5.6696 \times 10^{-8} W/m^2 \cdot K^4$ (Ch. VII)
τ	Fourier number
τ	input heat flux time parameter (s) (Ch. VII)
φ	inclination angle
ϕ	angle between two beams
	cylindrical coordinates azimuthal direction (*radians*) (Ch. VII)
θ	liquid contact angle
ω	oscillation frequency

SUBSCRIPTS

a	adiabatic region
a,b	mixture components
c	condenser region
cap	capillary
e	environment radiation sink (Ch. VII)
	evaporator region
eff	effective
f	fluid

g	gravity
in	input
j	wavelength 457.9 nm
k	wavelength 632.8 nm
l	liquid
lv	liquid-vapor interface
max	maximum
out	output
p	particle
	wick pore (Ch. VII)
rad	radiation
s	liquid-vapor interface
sat	saturation
son	sonic
v	vapor
w	pipe wall

ACKNOWLEDGMENTS

Abstract

The vapor flow in a heat pipe was mathematically modeled and the equations governing the transient behavior of the core were solved numerically. The modeled vapor flow is transient, axisymmetric (or two dimensional) compressible viscous flow in a closed chamber. The two methods of solution are described. The more promising method failed (a mixed Galerkin finite difference method) whereas a more common finite difference method was successful. Preliminary results are presented showing that multi-dimensional flows need to be treated.

A model of the liquid phase of a high temperature heat pipe was developed. The model is intended to be coupled to a vapor phase model for the complete solution of the heat pipe problem. The mathematical equations are formulated consistent with physical processes while allowing a computationally efficient solution. The model simulates time dependent characteristics of concern to the liquid phase including input phase change, output heat fluxes, liquid temperatures, container temperatures, liquid velocities and liquid pressures. Preliminary results were obtained for two heat pipe startup cases. The heat pipe studied used lithium as the working fluid and an annular wick configuration. Recommendations for implementation based on the results obtained are presented.

Experimental studies were initiated using a rectangular heat pipe. Both twin beam laser holography and laser Doppler anemometry were investigated. Preliminary experiments were completed and results are reported.

Chapter I

INTRODUCTION

A heat pipe is a device which transfers heat by evaporating and condensing a fluid. A wick structure is used to return the liquid to the evaporation zone by capillary effect. Figure 1 shows a typical sketch of a heat pipe which consists of the case, the wick structure and the vapor space. The input heat at one end of the pipe increases the temperature of the liquid in the wick structure. The liquid then evaporates, the pressure in the vapor core increases and the vapor flows to the other end. At this end the temperature is lower and the vapor condenses and releases heat. The liquid, then, flows from the condenser to the evaporator by capillary action through the wick structure.

The heat pipe is considered as a heat transfer device with very high conductivity. It can operate in weightless environments and transfer a huge amount of heat under conditions of very low temperature differences. These advantages make the heat pipe unique in space applications, electronic cooling systems and fusion energy systems. Although the steady state operation of heat pipe is well established, the transient behavior is not entirely well understood.

The reliability of a heat pipe for space applications depends on its ability to respond to a sudden change in the heat load, and startup and shut down of the thermal system. A comprehensive experimental and theoretical study is
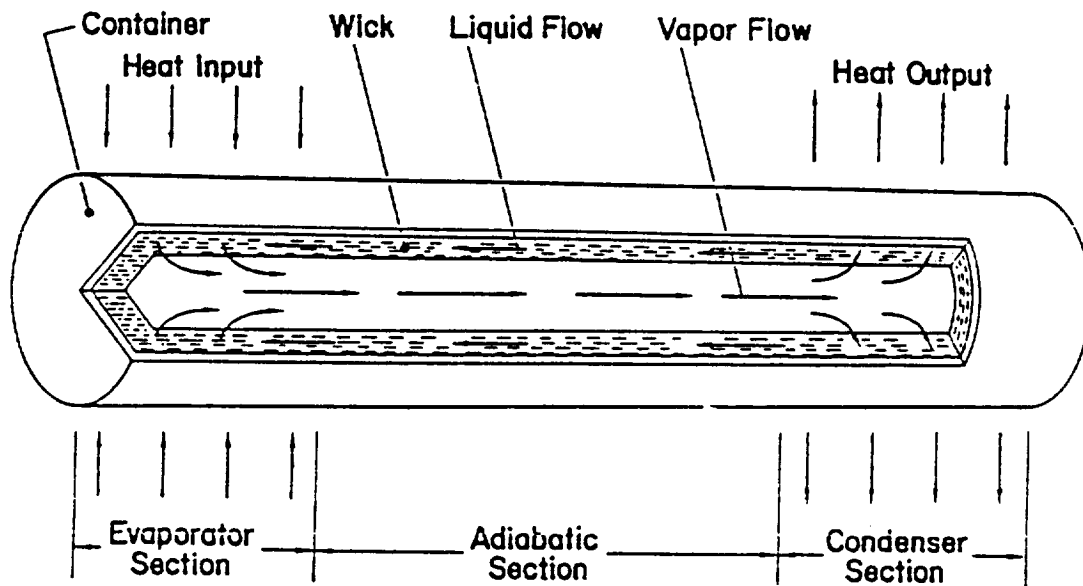
Figure 1:   A Heat Pipe

needed to understand and properly model the physical phenomena which occur in heat pipes during operational transients.

The objectives of this work were to investigate the dynamic behavior of the vapor flow in heat pipes, experimentally and theoretically. Experiments were to be carried out using a planar heat pipe to examine the transient response of the vapor core to a sudden increase in the input heat flux. Optical methods, which do not interfere the physical process, were proposed for measurements of velocity and temperature fields. The experimental apparatus and the optical methods are described in Chapter V.

The vapor flow in a heat pipe was mathematically modeled and the equations governing the transient behavior of the vapor core were solved nu-

merically. The modeled vapor flow is a transient, axisymmetric (or two-dimensional), compressible, viscous flow in a closed chamber. The boundary conditions include inflow and outflow of heat and mass which simulate the boundaries of the vapor core in a heat pipe. The proposed numerical method, along with preliminary results, are discussed in Chapter VI. The liquid phase is considered in Chapter VII.

The proposed objectives of the study were not fully met. Computer models were developed only to the state where feasibility of an approach was demonstrated. An experimental apparatus was built and put through some preliminary shake down testing. Much remains to be done to satisfy the objectives. This, of necessity, is left to others.

Chapter II

APPLICATIONS OF HEAT PIPES

Gaugler [1] was the first to develop the concept of a heat pipe in 1942 proposing to apply heat pipes for cooling the interior of an ice box. Later in 1964, an intensive work in this field was started by Grover and his coworkers [2] at the Los Alamos National Laboratory. The objective was the application of the heat pipe in spacecraft designs. The first quantitative analysis of heat pipes was performed by Cotter in 1965 [3]. Since then there have been many advances in theory, design and practice of heat pipes.

The fact that heat pipes are able to operate under very low gravity conditions and that they do not include any moving parts, has motivated the development of the heat pipe for space applications. In these applications the temperature is very high (1000- 2000°C) and liquid metals (such as sodium, lithium) are used as working fluids.

A heat pipe was proposed by Grover [2] to supply heat to the emitters of thermionic electrical generators and to remove heat from the collectors of these devices. In space based nuclear power systems, heat pipes are considered as a means to transfer heat from the generating point to the radiators and also to transfer heat throughout the radiators, providing a uniform temperature on the radiator surfaces [4].

4

Recently heat pipes have been proposed to be used in internal cooling of the leading edges of reentry vehicles and hypersonic aircrafts to reduce the peak temperature and alleviate the thermal gradients at the edge [5]. In this case the working fluid (a liquid metal) which is initially in the solid state, is melted by the reentry heat load and the heat pipe operation is initiated. The use of high temperature heat pipes as a heat transfer device has also been considered in rocket engines to cool and make the nozzles isothermal [6].

In case of a loss of coolant accident in a fusion reactor, it is desirable to ensure that no first wall melting or evaporation occurs. Such melting or evaporation of constituent elements can lead to the dispersal of radioactive waste hazards. In contrast to fission systems, a fusion power core usually contains enough thermal capacity to distribute the after-heat efficiently. Since the major component of decay after-heat is within a thin zone close to the first wall structure, a design incorporating heat pipes would result in an effective and fast redistribution of the decay after-heat. A heat pipe with a proper working fluid may be chosen such that the mechanism of heat transport through the pipe will start above a threshold design temperature. This would make the heat pipe operative only when needed, that is in the case of a loss of coolant accident.

Chapter III

THEORETICAL BACKGROUND

Theory of heat pipe operation is briefly outlined in this section. Pressure drop and heat flux in a heat pipe are discussed for engineering calculations along with the limits on the heat pipe operation. The section is ended with discussion of the transient operations of heat pipes. The detailed explanation of heat pipe theory may be found in Dunn and Reay [7].

3.1 PRESSURE DROP

In order for heat pipes to operate, the capillary driving force in the wick, Δp_{cap}, must overcome the pressure drop in the liquid phase, Δp_l, in the vapor phase, Δp_v, and the gravitational head, if any, Δp_g. That is

$$\Delta p_{cap} \geq \Delta p_l + \Delta p_v + \Delta p_g \tag{1}$$

The pressure difference across the interface of liquid and vapor is

$$\Delta p = \frac{2\sigma \cos \theta}{r} \tag{2}$$

where σ is the surface tension, θ is the contact angle, and r is the radius of curvature.

Figure 2 illustrates the operational conditions of the vapor-liquid interface. The radius of curvature in the condenser section is very large, whereas evapo-

ration causes the radius of curvature at the evaporator meniscii to decrease.
The difference between the radii of curvature in condenser and evaporator,
provides the capillary force. Thus, the capillary driving force, using Eq. 2, is

$$\Delta p_{cap} = 2\sigma\left(\frac{\cos\theta_e}{r_e} - \frac{\cos\theta_c}{r_c}\right)$$ (3)

where the subscripts e and c refer to evaportator and condenser, respectively,
and r is the radius of the capillary pore. Usually r_c is very large with respect
to r_e. This yields

$$\Delta p_{cap} = \frac{2\sigma\cos\theta}{r_e}$$ (4)
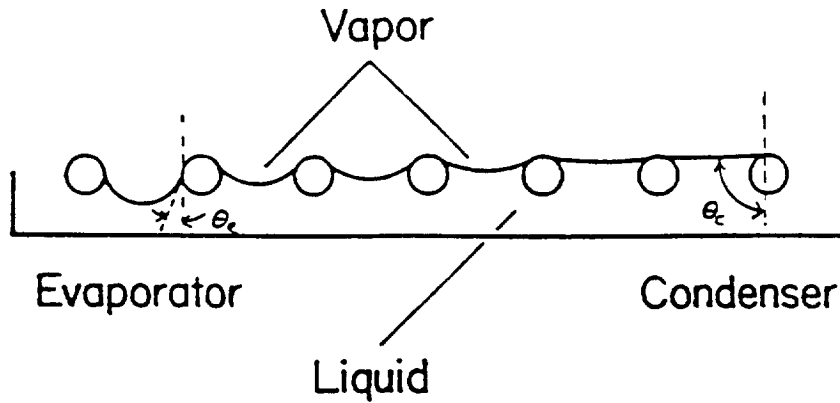
Figure 2:   Operational Level of Interface Between Liquid and Vapor

Pressure drop in the liquid phase, Δp_l, depends mainly on the structure of
the wick and the properties of the liquid. For engineering calculations the
liquid phase is modeled as a liquid flow in a porous medium. Since the mass

7

flow in the evaporator and condenser is not constant, an effective length, l_{eff}, is defined for the porous medium. The effective length, through which the mass flow is constant, is approximated as

$$l_{eff} = l_a + (l_e + l_c)/2 \qquad (5)$$

where l_a is the length of the adiabatic section which is between the evaporator and condenser sections. l_e and l_c are the lengths of the evaporator and condenser. Thus, Darcy's law is used to relate the pressure drop in the liquid phase to the wick and liquid properties, i.e.,

$$\Delta p_l = \frac{\mu_l \, l_{eff} \, \dot{m}}{\rho_l \, K \, A_w} \qquad (6)$$

where μ_l and ρ_l are viscosity and density of the liquid, $\dot{m}$ is the liquid flow rate, A_w is the wick cross sectional area and K is the wick permability given by

$$K = \frac{2 \, \varepsilon \, r_h^2}{f_l \, Re_l}$$

where ε is the wick porosity, r_h is the hydraulic radius and $f_l \, Re_l$ is the friction factor-Reynolds number product for laminar duct flow. The values of K for different types of wick structure is tabulated in Chi [8].

The pressure drop in the vapor phase, Δp_v, consists of the pressure drop in the adiabatic section, Δp_{va}, and the pressure drop in the evaporator, Δp_{ve} and in the condenser, Δp_{vc}. That is,

$$\Delta p_v = \Delta p_{va} + \Delta p_{ve} + \Delta p_{vc} \qquad (7)$$

In order to calculate for the pressure drop in the adiabatic section. the vapor flow in this region is assumed to be laminar Poiseuille flow in a circular tube [7]. Then the pressure drop Δp_{va}, is given by

$$\Delta p_{va} = \frac{8\mu_v \dot{m} l_a}{\pi \rho_v r_v^4} \tag{8}$$

where r_v is the radius of the vapor core. Applying a one-dimensional analysis Cotter [3] calculated the pressure drop in the evaporator and condenser, which are formulated as

$$\Delta p_{ve} = \frac{\dot{m}^2}{8\rho_v r_v^4} \tag{9a}$$

$$\Delta p_{vc} = \frac{-\dot{m}^2}{2\pi^2 \rho_v r_v^4} \tag{9b}$$

Upon substituting Eqs. (8) and (9) in Eq. (7), we get

$$\Delta p_v = \frac{8\mu_v \dot{m} l_a}{\pi \rho_v r_v^4} + 0.074 \frac{\dot{m}^2}{\rho_v r_v^4} \tag{10}$$

However, Busse [9], by using a modified Poiseuille velocity profile in Navier-Stokes equations, has shown that Δp_v can be expressed as

$$\Delta p_v = \frac{8\mu_v \dot{m} l_{eff}}{\pi \rho_v r_v^4} \tag{11}$$

where l_{eff} is defined in Eq. (5).

9

The hydrostatic head, Δp_g, is written as

$$\Delta p_g = g\,\rho_l\,L\,\sin\varphi \qquad (12)$$

where φ is the inclination angle of the heat pipe and L is the total length of the heat pipe.

Upon substituting Eqs. (6), (11) and (12) into Eq. (1), the circulation rate, $\dot{m}$, is given by

$$\dot{m} = \frac{\Delta p_{cap} - g\rho_l L\,\sin\varphi}{l_{eff}\left(\dfrac{\mu_l}{\rho_l K A_w} + \dfrac{8\mu_v}{\pi\rho_v r_v^4}\right)} \qquad (13)$$

3.2 HEAT FLUX

Neglecting the sensible heat which is small compared to the latent heat, the axial heat flux rate, q, is given by

$$q = \dot{m}\,h_{fg} \qquad (14)$$

where, $\dot{m}$ is the circulation rate of the working fluid and h_{fg} is the latent heat of evaporation.

From Eqs. (13) and (14) the heat transfer rate can be expressed as a function of the capillary driving force, the geometry and the properties of the working fluid; i.e.,

$$q = \frac{\left(\Delta p_{cap} - g\rho_l L \sin \varphi\right) h_{fg}}{l_{eff}\left(\dfrac{\mu_l}{\rho_l K A_w} + \dfrac{8\mu_v}{\pi \rho_v r_v^4}\right)} \qquad (15)$$

3.3 LIMITATIONS

There are several limitations on the output heat transported through heat pipes. These limitations are briefly described below.

1. Viscous limit: In long pipes and at low temperatures, the vapor pressure is low and the effect of viscous friction on the vapor flow may dominates over the inertial forces. In this situation the circulation of the working fluid is limited, which consequently, limits the heat transfer through the pipe.

2. Sonic limit: At low vapor pressures, the velocity of the vapor at the exit of the evaporator may reach the speed of sound. Then the evaporator cannot respond to further decrease in the condenser pressure. That is, the vapor flow is chocked, which limits the vapor flow rate.

3. Capillary limit: A capillary structure is able to provide circulation of a given fluid up to a certain limit. This limit depends on the permability of the wick structure and the properties of the working fluid.

4. Entrainment limit: The vapor flow exerts a shear force on the liquid in the wick which flows opposite the direction of the vapor flow. If the shear force exceeds the resistive surface tension of the liquid, the vapor flow entrains small liquid droplets (Kelvin-Helmholtz instabilities). The entrainment of liquid increases the fluid circulation but not the heat transfer through the pipe. If the

11

capillary force cannot accommodate the increased flow, dryout of the wick in evaporator may occur.

5. *Boiling limit:* At high temperatures, nucleate boiling may take place which produces vapor bubbles in the liquid layer. The bubbles may block the wick pores and decrease the vapor flow. Furthermore, the presence of bubbles decreases the conduction of heat through the liquid layer which limits the heat transfer from the heat pipe shell to the liquid which is by conduction only.

Heat Flow Limits

(1-2) Viscous
(2-3) Sonic
(3-4) Entrainment
(4-5) Wicking
(5-6) Boiling
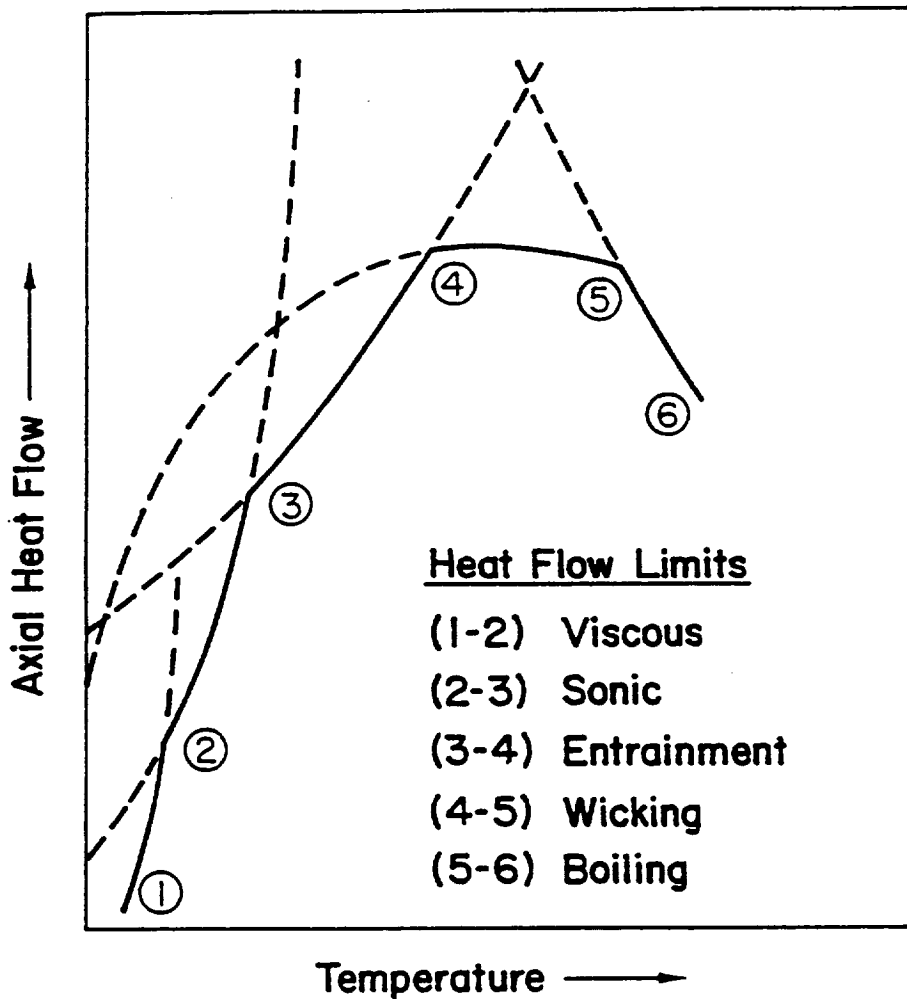
Figure 3: Heat Pipe Operating Limits

The above limits are fully explained in several textbooks (for example, Chi [8]) and are not reviewed here. These limitations dictate the operational envelope for a given design of a heat pipe, as shown diagramatically in Fig. 3 [2]. The shape of the operational envelope changes for different working fluids and different wick materials.

3.4 TRANSIENT OPERATION

Transient operation of heat pipes may be considered in terms of three different regimes: startup, operating transients and shut down. The following is a brief description of these regimes.

Startup

Heat pipe startup is a transient operation through which the heat pipe starts its operation from an initial static condition. The working fluid of heat pipe may initially be very cold or frozen in the wick. Under this condition, the vapor pressure is very low and the vapor flow is free molecular. The heat transfered from the evaporator melts the frozen working fluid in the evaporator and evaporation takes place in the liquid-vapor interface. The vapor pressure is initially very low and the vapor flow is highly accelerated. Then the flow may be chocked at the exit from the evaporation zone if its velocity reaches the sonic velocity. By addition of heat, the frozen working fluid is completely melted and a continuum vapor flow prevails throughout the vapor core.

Behavior of the vapor flow during the startup of a heat pipe from a frozen state, may be considered in three distinct phases: (*i*) free molecular flow throughout the vapor core, (*ii*) establishment of continuum flow in the evaporation zone with a front, moving towards the condenser with possibility of chocked flow at the evaporator exit and (*iii*) continuum flow of vapor all through the vapor core.

Operating Transients

Operating transients involve power changes during nominal operating conditions. There are several transient conditions of interest. A heat pipe may operate in a low power stand-by mode but be required to quickly respond to reach full power operation. A heat pipe may also be required to perform under load-following conditions, which depend on changing demands of the power conversion system. A nuclear reactor control system may also require changes in heat generation that would have to be handled by the heat pipe system.

The physics of interest for these situations depend on the initial conditions, the rate of change and magnitude of input power and condenser conditions. A heat pipe operating in stand-by mode at low vapor pressure may encounter the sonic limit while powering up. Large temperature gradients and complex vapor dynamics would develop. After passing through the sonic-limited operation, or for a heat pipe initially operating at high vapor pressure, the capillary, entrainment and boiling limits are of concern.

Shut Down

Shut-down of a heat pipe refers to the transient process occurring when the power of the thermal system is shut-off. The input heat of the heat pipe is

14

suddenly reduced to zero and the pipe cools down to a static condition. There are several problems encountered with this mode of transient operation. After the power is shut off, the working fluid of the heat pipe cools down and eventually solidifies. This phase change may affect the wick structure. The screen sheets of the wick are very delicate structures with fine meshes. Freezing of the working fluid in the screen holes may damage the wick structure by tearing the screen. Also if for some reason, the working fluid freezes mainly inside the screen holes, it will cause a major reduction in the driving force of the liquid flow.

Another possible problem is the appearance of cracks or bubbles in the solidified mass of the working fluid. The presence of cracks or bubbles can decrease the conduction of heat in the solidified mass during the startup, thereby the subsequent startup time increases. Cracks can also cause strain on the structure of the heat pipe and the screen and fatigue may become a serious problem after many shut downs. A proper heat pipe design must take into account the problems involved in the shut down transient mode, in order to have a reliable and long lasting heat pipe.

Chapter IV

LITERATURE REVIEW

The heat pipe studies were initiated by the experimental work of Grover et al. [2] and the quantitative analysis of Cotter [3]. Initial qualitative experiments were performed on heat pipes with water and sodium as working fluids. Cotter considered a right circular heat pipe with large length-to-diameter ratio. He performed a simple one-dimensional analysis on the vapor flow to develop the general basic theory for quantitative engineering calculations of heat pipe operations. These studies have been continued to develop the theory and performance of heat pipes.

The vapor flow in heat pipes is a complicated problem due to high nonlinear character of the governing equations and the inflow and outflow boundaries in the evaporator and condenser. Different approaches have been used to simplify the problem. In most of the work done so far, the vapor flow is analyzed under steady state conditions, as a one dimensional flow [10,11,12,13] or a two dimensional flow [14-24].

Banskton and Smith [14,15] developed numerical solutions for incompressible, steady state, two dimensional vapor flow in a heat pipe. Their results show flow reversal in the condenser for radial Reynolds numbers larger than two. Indication of a reverse flow is important in design of a heat pipe in calculating the shear forces acting on the wick structure. Flow reversal may

also affect the entrainment limit. They also found that the pressure profiles across the heat pipe were two dimensional. Their study recommended the solution of the complete (compressible) two dimensional Navier-Stokes equations to provide an accurate prediction of the pressure drop along the pipe.

McDonald et al. [16] analyzed a vapor flow in an enclosure in the presence of air as a noncondensible gas. The coupled governing equations for steady state two dimensional flow were numerically solved to study the effects of air on the evaporation and condensation rates of the water heat pipe. They concluded that the two dimensionality of the flow field had a very small effect on the concentration of the noncondensible gas and on the temperature distributions in the vapor core.

However, Rohani and Tien [17,18] showed that in liquid metal gas loaded heat pipes, a one-dimensional analysis is not adequate. This conclusion was explained by averaging the two-dimensional results over the cross section, and comparing these with those of one-dimensional analysis [15]. They performed a numerical analysis of the steady state two dimensional heat and mass transfer in the vapor gas region of a gas loaded heat pipe. Their results show that the vapor flow in the vicinity of the vapor-gas front is negligibly small and they concluded that heat and mass are transfered only by conduction and diffusion at the front. But, in an analysis done by Peterson and Tien [19] it was shown that natural convection and radial diffusion have a significant effect on the noncondensible gas distribution in the vicinity of the vapor-gas front.

17

Gas controlled heat pipes (GCHP) were recently investigated by Galaktionov and his colleagues from the Moscow Energy Institute [20,21]. In their analysis, they included convection and diffusion across the front under heat loads considerably smaller than the sonic limit of heat pipe operation. Galaktionov et al. [20] presented a mathematical model for incompressible, steady state, two dimensional problem for the heat and mass transfer in the region of the vapor-gas front in a GCHP. In their analysis, using boundary layer assumptions in the evaporator zone, they applied an integral method and approximated the axial velocity by a fourth-order polinomial.

The same problem was analyzed by Galaktionov and Trukhanova [21], taking into account the compressibility of the vapor. By defining a stream function for the velocity field, the momentum equation was written in terms of the vorticity and stream function. The governing equations were solved numerically by the Gauss-Seidel method. They also carried out experimental studies of a planar gas controlled heat pipe. The results show that the variations of temperature in axial and radial directions are quite comparable, which clearly demonstrate the two dimensional character of the problem. The velocity profiles show the reverse flows in the region of the vapor-gas front.

Reverse flow in the condenser section was also observed by Ooijen and Hoogindoorn [22] who performed experimental and numerical studies on heat pipe vapor flow. Their analysis was confined to a steady state, incompressible, two dimensional flow. They also found that the total pressure drop over the heat pipe, for high radial Reynolds numbers, was higher than that approximated by a Poiseuille flow model.

Narayana [23] performed a numerical study of incompressible, steady state, two dimensional vapor flow. He showed that the pressure terms in the Navier-Stokes equations could be eliminated by integrating the momentum equation in the axial direction, on the pipe cross section. In this analysis, using boundary layer assumptions, the radial pressure variation was neglected.

A double-walled concentric heat pipe was proposed by Faghri [24]. Two pipes with different diameters create an annular space for the vapor flow. The wick structures are attached to the inner surface of the outer pipe and the outer surface of the inner pipe. In this kind of heat pipe the area of heat transfer into and out of the pipe is increased and its efficiency of performance is expected to be higher. Faghri has carried out a numerical study of the vapor flow in such a double-walled heat pipe. He used an implicit marching finite difference method to solve the incompressible, steady state, two dimensional flow problem. His results show that for low Reynolds numbers, viscous effects dominate. For radial Reynolds numbers greater than one, pressure decreases in the vapor flow direction in the evaporator section, whereas it increases in the condenser section due to partial dynamic pressure recovery from the decelerating flow. For high radial Reynolds numbers, flow reversal flow was shown to occur in the condenser section.

In studies of the dynamic behavior of heat pipes, three different areas of concern are startup, shut down and operating transients. Among these the startup mode of transient is the most difficult one. As mentioned above, the startup of a heat pipe may be encountered with melting of the working fluid

19

at solid state, free molecular flow of vapor and dry out and rewetting of the wick.

Extensive studies of startup and shut down operations of heat pipes [25,26,27,28,29] have been carried out at the Los Alamos National Laboratory. The objectives were the applications of high temperature, liquid metal heat pipes to space power system heat rejection. Experiments were performed on a long heat pipe with a molybdenum container. Using liquid sodium and potassium as working fluids, design characteristics of high temperature heat pipes have been evaluated. For the temperature range of 700 to 1600 K, the useable length of 30m with length-to-diameter ratio of 300 was found for potassium heat pipes, whereas for sodium heat pipes useful lengths of more than 40m with length-to-diameter ratio of 800 were predicted.

In the numerical studies [29], heat pipe performance was modeled to include startup from the frozen state of the working fluid, with provision for free molecule flow of the vapor. Vapor core dynamics were simulated by a transient one dimensional compressible flow with friction and mass flow from the wick. The governing equations were solved using the KACHINA method [30]. The numerical code is still under development. In the present status it requires 30 minutes of Cray computational time per hour of actual time.

Bystrov and Goncharov [31] performed experimental and theoretical studies on a heat pipe with and without a foreign gas. The steady state operation and startup from a frozen state of liquid were analyzed. By averaging across the axial cross section, they solved unsteady, one dimensional equations for the vapor and liquid phases. Their numerical scheme could be run only for

very small time steps (10^{-5} to 10^{-7} sec) due to stability problems and as a result needed a large amount of computational time. In order to increase the time steps, they used a lumped parameter approach for heat balance and avoided calculations of detailed temperature distributions.

Chang and Colwell [32,33,34] studied the transient operation of low temperature heat pipes experimentally and numerically. Experiments were performed with Freon 11 as a working fluid to study the dryout and rewetting of the liquid phase. In their analysis the vapor core temperature was assumed to vary only with time, allowing the solution of a two dimensional conduction problem for the liquid and wick structure.

Ambrose et al. [35] studied pulsed startup of heat pipes. A pulsed startup refers to applying a step increase in input heat flux to a heat pipe under steady state conditions. They performed experiments on a simple-screen-wicked copper-water heat pipe to investigate the transient time and the dryout and rewetting behavior. The transient time was found to be dependent on the capillary force, the cooling mechanism and the heat capacity of the pipe. Dryout of the wick at the evaporator was found to occur only for heat fluxes greater than the capillary limit. Dryout and rewetting were modeled using a lumped parameter method. Good agreement between the experimental data and the theoretical results was reported.

The works done so far on the transient behavior of heat pipes, mainly concern startup and shut down operations. However, these modes of transient are still not well established. Furthermore, no major work has been done on the operating transients heat pipes are expected to undergo. For a comprehensive

study of the dynamics of heat pipes, the vapor flow needs to be thoroughly investigated both theoretically and experimentally.

Previous theoretical studies of dynamics of compressible vapor flow have considered a transient one-dimensional model. In these studies the friction coefficients of the vapor flow boundaries, have been approximated using a steady state two-dimensional model. In addition, steady state two-dimensional analyses have shown that one-dimensional models of the vapor flow are not able to accurately predict the axial heat and mass transfer and the axial pressure drops. Furthermore, two-dimensional steady state studies indicate that flow reversal takes place in the condenser section. It is, therefore, important to establish the conditions under which this mode occurs during transient operations.

Chapter V

PROPOSED EXPERIMENTS

Transient behavior of the heat pipe internal flows needs to be examined experimentally to understand and properly model the physical phenomena governing their behavior. In applications such as space based nuclear power systems, it is desirable to know how fast the heat pipe reacts to a sudden ramp in input power. In this section the experimental setup is described and the proposed methods of measurement are discussed.

5.1 EXPERIMENTAL APPARATUS

Figure 4 shows a schematic diagram of the experimental apparatus. A rectangular pipe has been designed and built to simulate a heat pipe. The bottom of the pipe is a plane wide thin channel which contains the working fluid. Two layers of stainless steel mesh (300 series, 400 mesh) are fixed on top of the liquid channel to serve as the wick structure. The axial sides of the pipe are made of glass to permit flow visualization. The top of the pipe is insulated. One end of the bottom plate is heated by patch heaters which supply up to 1.55 w/cm^2. The other end is cooled by air flow. The middle region of the bottom plate is insulated to approximate the adiabatic conditions.

Freon 11 and Freon 113 are chosen as working fluids. These fluids have low latent heat, low boiling point and are easy to handle. The low latent heat

allows one to induce a liquid-vapor phase transition at low applied heat fluxes. A scaling analysis can be used to generalize the results to other fluids.

Axial and vertical velocity components will be measured using Laser Doppler Anemometry. The temperature and concentration profiles in the vapor core are measured simultaneously using twin beam laser holographic interferometry. These methods are described briefly in the following sections.
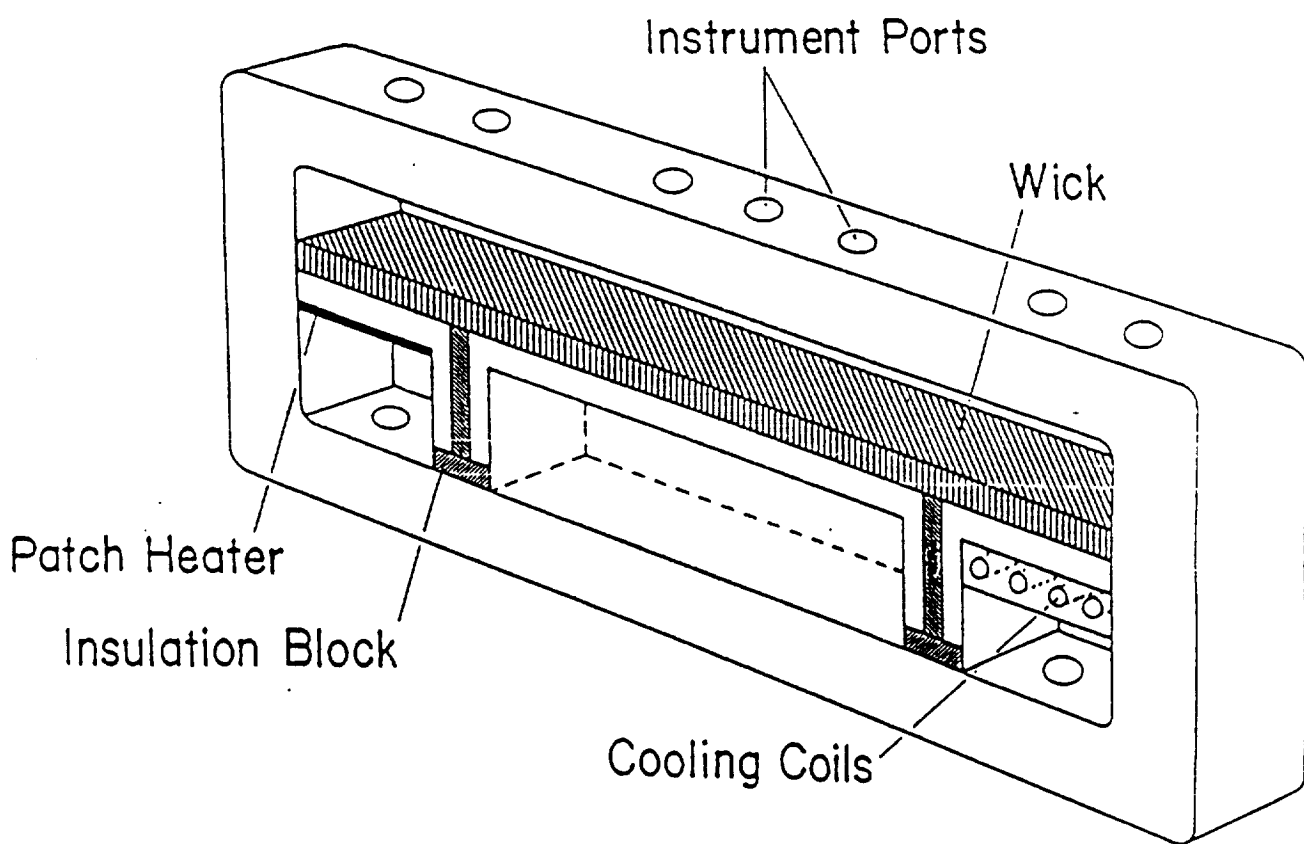

Figure 4: Experimental Rectangular Heat Pipe

5.2 OPTICAL METHODS

Optical methods have been used for many years in heat and mass transfer measurements due their unique advantages. These methods do not disturb the examined process and the information of the whole field is recorded on photographs which has advantages over methods of point by point measurements. Furthermore, the measurements are inertialess and therefore, very fast phenomena can be investigated [36].

In this section, the use of optical methods in heat pipe experiments are discussed. Laser Doppler anemometry is proposed for measuring the axial and vertical velocity components of vapor flow. The advantages of twin beam holographic interferometry are discussed as a means of simultaneously measuring both the temperature and concentration distributions in the vapor core.

5.2.1 *Holographic Interferometry*

Interferometric methods are based on differences in lengths of the optical paths. Among these methods, holographic interferometry is the least expensive and easiest to construct with a comparative accuracy [36]. However, a highly coherent light is needed. The single beam holographic interferometry is first illustrated. Then it will be shown how this method can be modified to twin beam interferometry.

Single Beam Interferometry

Figure 5 is a schematic diagram of a single beam interferometer. The light source is a laser. The laser beam is split into an object beam and a reference

beam. Each beam is passed through a microscope objective and a collimating

lens and expanded to a parallel beam. The reference beam falls directly on the

hologram plate, whereas the object beam passes through the experimental ap-

paratus and then intersects the reference beam on the hologram plate.

In real-time holographic interferometry the photographic plate is exposed

before the experiment starts, and the comparison wave is recorded. The pho-

tograph plate is developed and fixed while it stays in its place. The comparison

beam is then reconstructed by illuminating the hologram with the reference

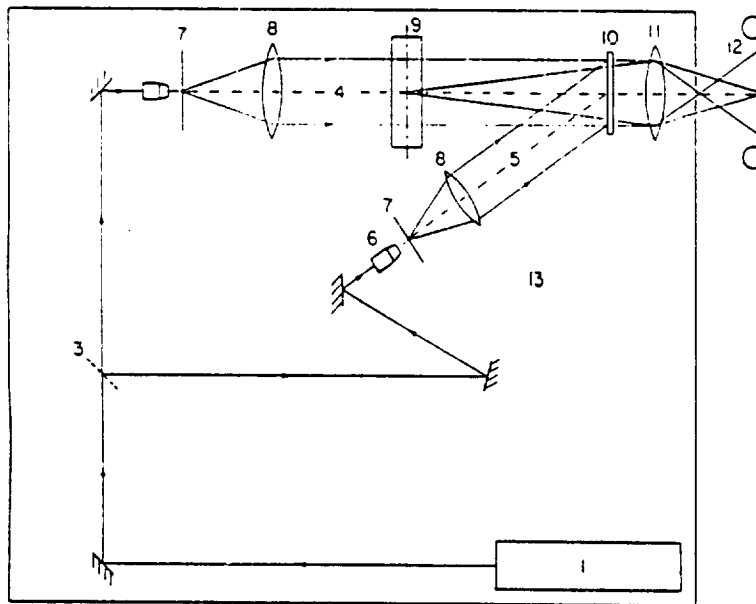beam. After the experiment starts a phase change occurs in the object beam

Figure 5: Schematic of Single Beam Holographic Interferometer
1. Helium-Neon Laser, 2. Argon Laser, 3. Variable Beam Splitter,
4. Object Beam, 5. Reference Beam, 6. Microscope, 7. Pinhole,
8. Collimating Lens, 9. Test Section, 10. Holographic Plate,
11. Lens, 12. Camera, 13. Air-Suspension Table, 14. Shutter

and illumination of this beam on the hologram produces interference fringes. Changes in the interference pattern due to changes in the process can be continuously observed or photographed.

Interferometric methods are based on the measurement of variations of the refractive index in the test section. These variations may be caused either by temperature, concentration or pressure gradient fields. Any of these fields alone can then be determined by evaluation of the interferogram. However, if the refractive index is changed due to temperature and concentration changes simultaneously, an interferogram produced by a single beam interferometer may not be adequate to evaluate the temperature and/or concentration fields. This difficulty can be overcome by using two laser beams with two different wavelengths. This method is called twin beam (or two-wavelength) holographic interferometry and was first proposed by Mayinger and Panknin [37].

Twin Beam Interferometry

The first accurate results were obtained by Panknin [38]. Using twin beam interferometry he found good results for measurement of the temperature and concentration in simultaneous heat and mass transfer along a heated vertical plate and a horizontal cylinder with sublimation and the temperature and fuel distributions in a flame.

Figure 6 shows the required experimental arrangement. The twin beam interferometer is very similar to that of the single beam shown in Fig. 5. Here, two lasers, an Argon laser $(\lambda_j = 457.9\,nm)$ and a Helium-Neon laser $(\lambda_k = 632.8\,nm)$ are used as light sources. The two beams lie on a horizontal

27

plane and are perpendicular to each other when they intersect on the beam splitter. Therefore, both object and reference beams consist of two different wavelengths.

The exposure technique in twin beam interferometry is similar to that of the single beam. Before the experiment is started, the comparison wave, which now consists of two wavelengths, is recorded on a photograph plate. The photograph plate is developed and fixed. Now, if the laser beam with the wavelength, say, λ_j , is blocked, both reference and object beams will have wavelength λ_k . Then by illuminating the reference beam on the hologram, the
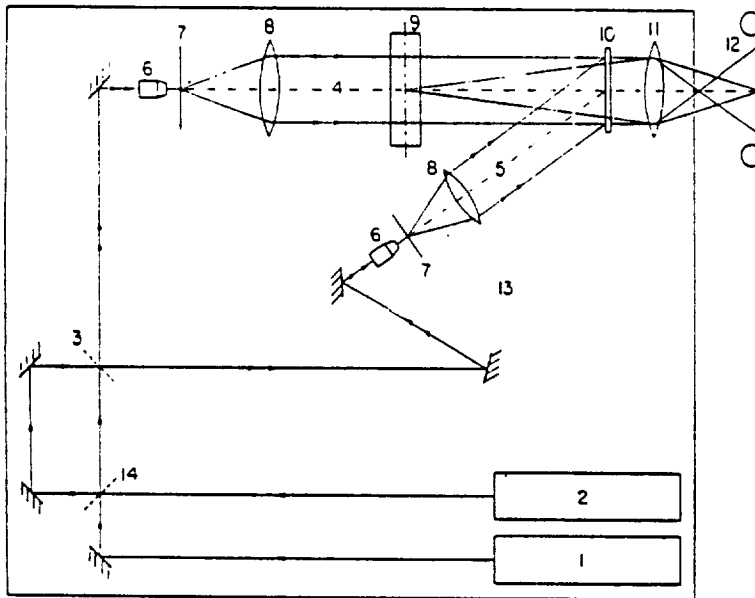

Figure 6:   Schematic of Twin Beam Holographic Interferometer
1. Helium-Neon Laser, 2. Argon Laser, 3. Variable Beam Splitter,
4. Object Beam, 5. Reference Beam, 6. Microscope, 7. Pinhole,
8. Collimating Lens, 9. Test Section, 10. Holographic Plate,
11. Lens, 12. Camera, 13. Air-Suspension Table, 14. Shutter

28

comparison wave is reconstructed. The object beam which passes through the test section is illuminated on the hologram and produces an interference pattern for wavelength λ_k . By shining the laser beam of wavelength λ_j , another interference pattern is produced for wavelength λ_j .

The main advantages of this technique is that only one plate is developed which includes information from both wavelengths, and two interference patterns are produced by shining each laser beam, separately. Two sets of fringes are, then, evaluated to determine the temperature and concentration profiles for the tested medium. The evaluation method of fringes is discussed in the following section.

5.2.2 *Theory of Twin Beam Interferometry*

The following assumptions are made in development of the governing equations [38]:

1. The optical system is perfect, the experimental setup is mechanically stable and the lasers are ideal.

2. The object beams with the wavelengths λ_j and λ_k are ideal parallel waves.

3. The variation of the refractive index is only two dimensional and no variation in the beam direction.

4. No reflection of beam due to gradients of the refractive index.

5. Refractive index is constant outside of the test section and during recording of the comparison waves.

29

6. The holographic construction is perfect.

With the above assumptions the interference pattern depends only on the variation of the refractive index. In holographic interferometry the object beam, passing through the test section at different times, is superimposed on the comparison wave, and therefore, reveal the difference in optical pathlengths in two exposures. Expressed in multiple S of the wavelength λ, this difference is written as

$$S(x,y,\lambda) \cdot \lambda = l\left\{n(x,y,\lambda) - n_\infty\right\} \tag{16}$$

where l is the width of the test section, in which the refractive index varies because of temperature and concentration gradients. The interference pattern shows the change of the refractive index between the recorded comparison wave (constant temperature T_∞ and constant concentration C_∞, yield a constant refractive n_∞) and the "measurement" wave.

An extinction of light occurs for

$$|S| = \frac{1}{2}, \frac{3}{2}, \frac{5}{2} \cdots \qquad \text{(dark fringes)} \tag{17}$$

and an amplification for

$$|S| = 1, 2, 3 \cdots \qquad \text{(bright fringes)} \tag{18}$$

The interference fringes are points of the same refractive index change. With temperature and concentration gradients the refractive index variation depends on both gradients. Therefore, a relationship has to be found between

the refractive index change due to the temperature gradient and that due to the concentration gradient.

The molar refractivity $N(\lambda)$, is related to the refractive index by the Lorentz-Lorenz equation as follows

$$N(\lambda) = \frac{n(\lambda)^2 - 1}{n(\lambda)^2 + 2} \cdot \frac{M}{\rho} \qquad (19)$$

where M is the molecular weight and ρ is the density. Fortunately the molar refractivity does not depend on temperature and pressure, but it varies with wavelength. This is the basis for the twin beam interferometry.

For gases with $n \simeq 1$, Eq. (19) is approximated quite accurately by the Gladstone-Dale equation

$$N(\lambda) = \frac{2M}{3\rho}[n(\lambda) - 1] \qquad (20)$$

For the ideal gases the density, ρ, can be replaced by the total pressure, p, and the temperature, T, to get

$$N(\lambda) = \frac{2RT}{3p}[n(\lambda) - 1] \qquad (21)$$

where R is the gas constant. The molar refractivity, $N(\lambda)$, for a mixture of two components is given by

$$N(\lambda) = C_a N_a(\lambda) + C_b N_b(\lambda) \qquad (22)$$

with $C_a + C_b = 1$. In the above equation C_a and C_b are the concentration of the components a and b in the mixture and $N_a(\lambda)$ and $N_b(\lambda)$ are the molar refractivity of the components in their pure form.

Combining Eqs. (16), (21), and (22) yields

$$S(x,y,\lambda) \cdot \lambda = \frac{3pl}{2R}\left\{\frac{1}{T(x,y)}\left[N_a(\lambda) + C_b(x,y)\,(N_b(\lambda) - N_a(\lambda))\right] - \frac{1}{T_\infty}N_a(\lambda)\right\} \quad (23)$$

with $C_a = 1 - C_b$, $C_{a,\infty} = 1$ and $C_{b,\infty} = 0$ (only component a presents in recording the comparison wave). For two different wavelengths λ_j and λ_k we get two equations from which the temperature and concentration distributions will be evaluated. These equations are the following

$$S(x,y,\lambda_j)\frac{\lambda_j}{\Delta N(\lambda_j)} - S(x,y,\lambda_k)\frac{\lambda_k}{\Delta N(\lambda_k)} =$$
$$-\frac{T(x,y) - T_\infty}{T(x,y) \cdot T_\infty}\frac{3pl}{2R}\left[\frac{N_a(\lambda_j)}{\Delta N(\lambda_j)} - \frac{N_a(\lambda_k)}{\Delta N(\lambda_k)}\right] \quad (24)$$

$$S(x,y,\lambda_j)\frac{\lambda_j}{N_a(\lambda_j)} - S(x,y,\lambda_k)\frac{\lambda_k}{N_a(\lambda_k)} =$$
$$\left[\frac{C(x,y)}{T(x,y)} - \frac{C_\infty}{T_\infty}\right] \cdot \frac{3pl}{2R}\left[\frac{\Delta N(\lambda_j)}{N_a(\lambda_j)} - \frac{\Delta N(\lambda_k)}{N_a(\lambda_k)}\right] \quad (25)$$

where $\Delta N(\lambda) = N_b(\lambda) - N_a(\lambda)$.

Figure 7 demonstrates how to evaluate the temperature profile, $T(y)$, and the concentration profile, $C(y)$, from two interferograms of a boundary layer produced by two different wavelengths, λ_j and λ_k [38]. For a specified direction along the boundary layer, $x = \text{constant}$, Fig. 7b shows S_j, S_k, $S_j \cdot \lambda_j$ and

$S_k \cdot \lambda_k$ as functions of y , where $S_j = S(x = \text{const}, y, \lambda_j)$ and

$S_k = S(x = \text{const}, y, \lambda_k)$. According to Eqs. (24) and (25) the temperature and

concentration profiles at a location are found by the following equations

$$T(y) - T_\infty \simeq \frac{S_j \cdot \lambda_j}{\Delta N_j} - \frac{S_k \cdot \lambda_k}{\Delta N'_k} \tag{26}$$

$$C(y) - C_\infty \simeq \frac{S_j \cdot \lambda_j}{N_j} - \frac{S_k \cdot \lambda_k}{N'_k} \tag{27}$$
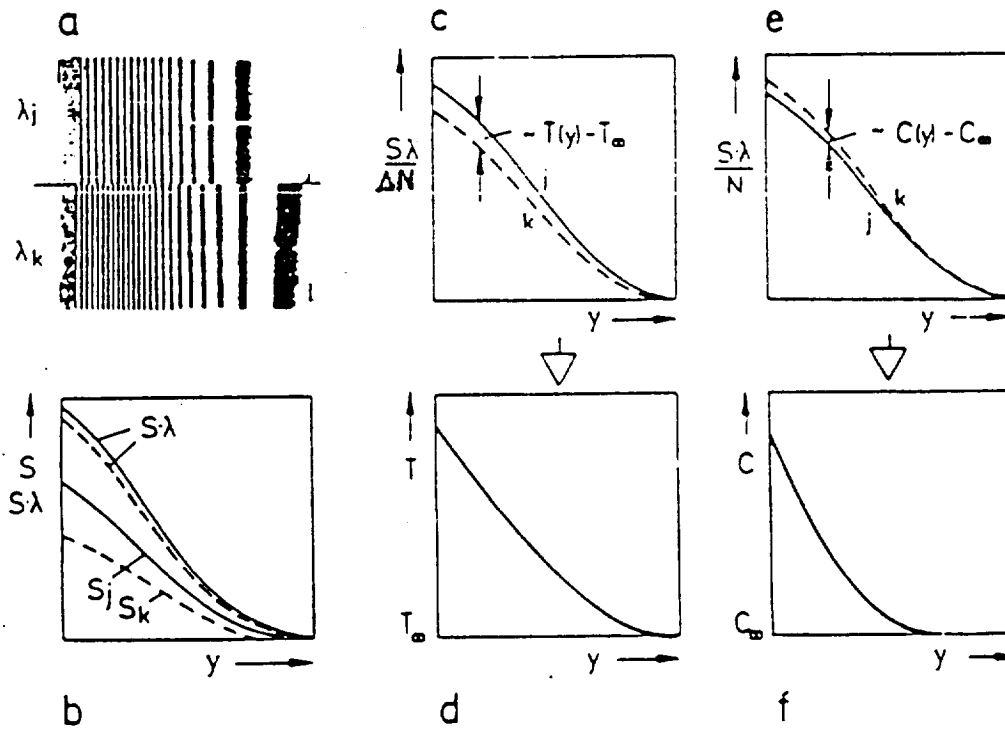
a) Interferograms for λ_j and λ_k
b) Phase lag $S \cdot \lambda$, S
c), e) Difference of modified phase lags
d), f) Temperature and concentration profiles

Figure 7:   Evaluation of Interferograms [38]

33

where $N_j = N_a(\lambda_j)$ and $N_k = N_a(\lambda_k)$. Figures 7c and 7e show the variations of $S \cdot \lambda / \Delta N$ and $S \cdot \lambda / N$ for λ_j and λ_k. Then using these distributions, Eqs. (26) and (27) yield the temperature and concentration profiles for that location. These profiles are shown in Figs. 7d and 7f.

5.2.3 Laser Doppler Anemometry

The laser Doppler anemometry allows the measurement of the local, instantaneous velocity of tracer particles suspended in a flow without disturbing the flow. Thus, appropriate particles must exist in the fluid and the relationship between the particles and fluid velocity must be known. The task of a laser Doppler anemometer falls into three parts.

- Generating two coherent laser beams which interfere in a probe volume

- Detecting the light intensity scattered by tracer particles crossing the measuring control volume

- Analysing the Doppler frequency and calculating the velocity of the particles

Figure 8 shows the required components of a laser Doppler anemometer and the following is a brief description of the basic principles of laser Doppler anemometry which are carefully outlined in Durst et al. [39].

Two coherent laser beams with wavelength λ and a diameter d form an ellipsoidal volume at the beam intersection point (see Figs. 9 and 10). The size of the measuring control volume is given by

34

$$\delta_x = d; \qquad \delta_y = \frac{d}{\sin\phi}; \qquad \delta_z = \frac{d}{\cos\phi} \qquad (28)$$

where ϕ is the angle between the two beams and δ_x, δ_y and δ_z are the axes of the ellipsoid. Figure 10 shows the principles of the "interference fringe" model which was proposed by Rudd [40].

Two coherent laser beams having plane wave fronts intersect at an angle, ϕ. This yields a pattern of plane interference fringes as shown in Figure 10. The fringe spacing, Δz, is proportional to the wavelength, λ, of the light and inversely proportional to the half angle between two beams

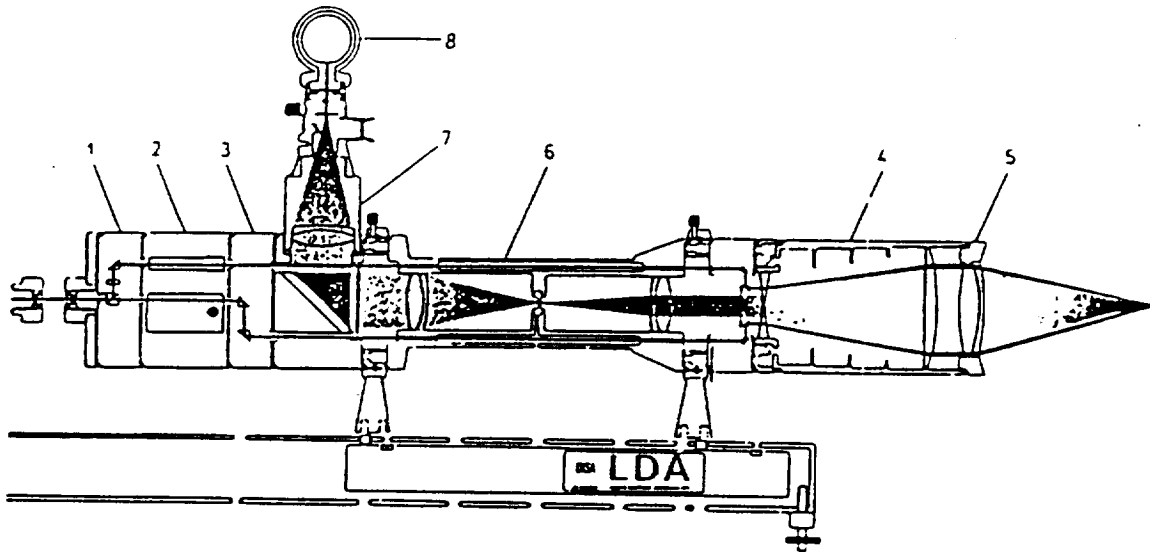$$\Delta z = \frac{\lambda}{2\sin(\phi/2)} \qquad (29)$$

Figure 8: LAD Optics from DANTEC Manual
1. Beam Splitter 2. Bragg Cell Unit 3. Beam Displacer
4. Beam Expander 5. Front Lens 6. Pinhole Unit
7. Photomultiplier Optics 8. Photomultiplier

As a particle moves through the region of interference fringes it will scatter light whose intensity will vary according to the light intensity variation inside the bisector of the two beams. These light intensity variations have the Doppler frequency ν_D given by

$$\nu_D = \frac{U}{\Delta z} = \frac{2 U \sin{(\phi/2)}}{\lambda} \qquad (30)$$

where U is the particle velocity component perpendicular to the fringes.

The scattered light can be detected by a photomultiplier and the velocity component normal to the interference fringes can be determined by analyzing the Doppler frequency. This frequency is ambiguous because it does not indicate in which direction a particle moves. This lack of information can yield large errors if the flow direction is not known (e.g. in case of recirculating flow)
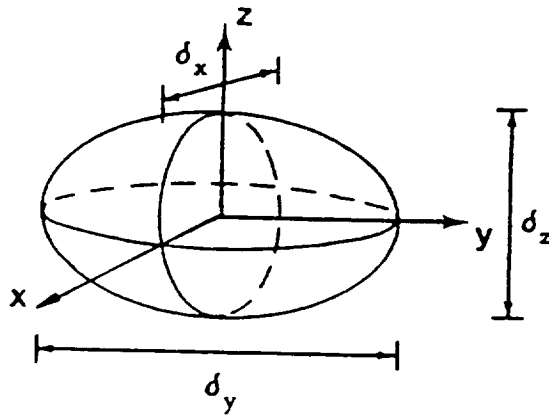
Figure 9: Measuring Control Volume

or if the mean velocity is near-zero and the fluctuations are larger than the mean value in turbulent flow.

Frequency shifting allows the 180 degree ambiguity in the direction of a measured velocity to be resolved. The frequency shift is obtained when the two intersecting laser-beams have different frequencies. The presence of a frequency difference, v_s, results in a movement of the fringe pattern with velocity U_s,

$$U_S = - v_S \Delta z \tag{31}$$

A frequency shift, applied to one of the laser beams, will result in an increase or decrease in the measured velocity of a particle depending on the direction of the movement. In this case the velocity can be determined clearly from the detected Doppler frequency, v_D. If the velocity of the fringes, caused by the shift frequency, is greater than the particle velocity

Figure 10: Interference Fringes in the Control Volume

37

$$U = (v_D - v_S) \frac{\lambda}{2 \sin(\phi/2)} \qquad (32)$$
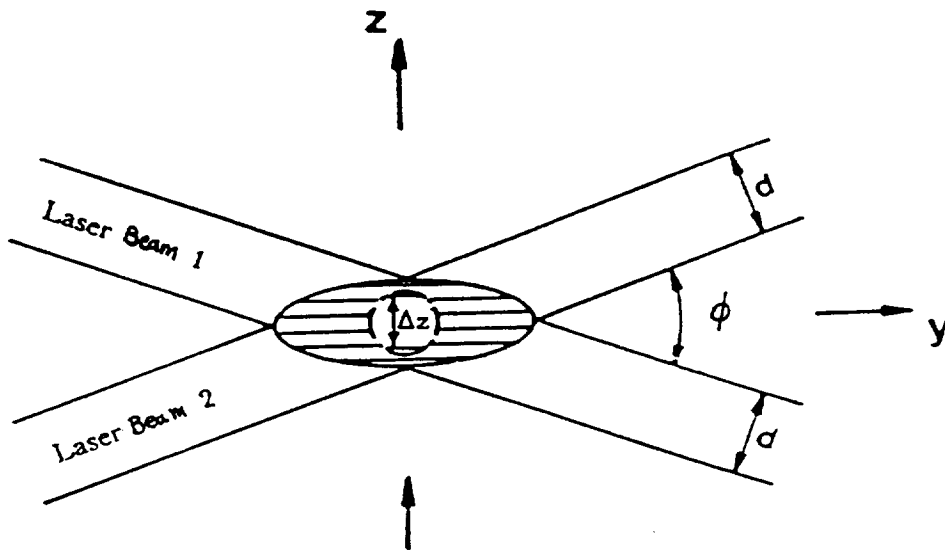
A lower Doppler-frequency than the shift frequency indicates that a particle moves in the same direction as the fringe pattern. If a particle moves in the opposite direction, the Doppler frequency will be larger than the shift frequency.

Laser Doppler anemometry depends on signals from particles suspended in the flow. Thus, it is important to know how well the motion of the particles represent the motion of the fluid. In our case there are two reasons for velocity differences:

- The particle terminal velocity is different from the vapor velocity because of greater gravitational forces on the particle as compared to the vapor.

- Drag forces caused by accelerations and velocity fluctuations can result in particle/vapor mismatch.

According to Tchen [41], the terminal velocity, C_t, of a particle in a fluid with the constant velocity U_f parallel to the gravity g is

$$U_p = U_f - C_t \qquad \text{with} \qquad C_t = \frac{2}{g} \frac{r_p^2}{\mu_f} (\rho_p - \rho_f) \qquad (33)$$

The velocity difference C_t between the particle U_p and the fluid U_f depends on the density difference, $\rho_p - \rho_f$, the viscosity of the fluid, μ_f, and the squared radius of the particles r_p^2. For oil droplets ($r_p \simeq 1 \mu m$) in gas, at standard state. $C_t \simeq 1.5 \cdot 10^{-4}$ m/s.

According to Dring [42] the velocity difference between a particle and fluid caused by high-frequency velocity oscillations, depends on the Stokes number

$$St = \frac{\rho_p \omega \, 4 r_p}{18 \mu_f} \tag{34}$$

For Stokes number St < 0.14 the particles follow an oscillation with the frequency ω with less than 1% velocity difference. For oil droplets in a gas, at standard states, $\omega_{max} \simeq$ 12 kHz.

5.3 PRELIMINARY RESULTS

Experiments have been carried out to visualize the vapor flow patterns in evaporation, adiabatic and condensation regions of the heat pipe after a sudden increase in input heat flux has been applied. A boundary layer of vapor is established very quickly on top of the wick surface all over the heat pipe. The thickness of this layer decreases from the evaporation section to the condensation region. The vapor boundary layer grows quickly and fills the whole space. Depending on the input heat flux, the whole process takes place in a few seconds. For low input heat flux, the vapor flow is found to be smooth and laminar. For higher heat fluxes the vapor boundary layer grows faster. If the input heat was high enough a few regular vortices were observed on top of the evaporation part and they expanded to the entrance region of the adiabatic part. The vapor flow in the adiabatic and condensation regions under a high heat flux are still laminar but reverse flow on top of the condenser is suspected.

Transient processes in the vapor core of heat pipes are very fast (few seconds). Therefore, the mentioned optical methods which provide inertialess measurements, are the proper tools to obtain accurate results. The temperature and concentration profiles are evaluated from the holograms developed by the twin beam interferometry. In this method, the temperature is evaluated from the difference between the phase shifts corresponding to two different wavelengths (see Eq. (26)). This difference is usually very small, therefore, the two wavelengths used should be as far apart as possible.

In laser Doppler anemometry, seeding of particles with proper density and size is a challenging problem. In systems like heat pipes, in which the working fluid undergoes a phase change, it is not possible to have particles recirculating with the fluid flow. In this case, particles can be injected carefully into the vapor flow in the evaporation end and collected from the condensation end. But the disadvantage of this technique is that the measured velocities at both ends are not accurate.

When the evaporation and condensation rates are high, small liquid droplets are present in the vapor flow. These droplets flow with the vapor and are able to scatter the laser beam. Preliminary velocity profiles in both the evaporator and condenser have been obtained to demonstrate that the method will be effective. Therefore, no seeding will be required in this case.

Chapter VI

THEORETICAL MODEL OF THE VAPOR CORE

Flow patterns found in a heat pipe are shown schematically in Fig. 11. The working fluid evaporates in the evaporation zone. The local pressure increases and the vapor flows towards the condensation zone, at which it condenses back to the liquid phase. The liquid flows from the condenser to the evaporator by capillary force through the wick structure. The main concern of this analysis is the vapor core response to changes in the evaporation and condensation rates due to a sudden increase, or decrease, in the input heat flux, or the condenser temperature.

In this section the dynamic behavior of the vapor flow is analysed using a transient two dimensional model. The proper equations which govern the model problem will be written. A numerical scheme will be proposed to solve the governing equations. Then, presenting some preliminary results of the numerical calculations, the continuation of the analysis to more rather complete solution of the problem, will be proposed.
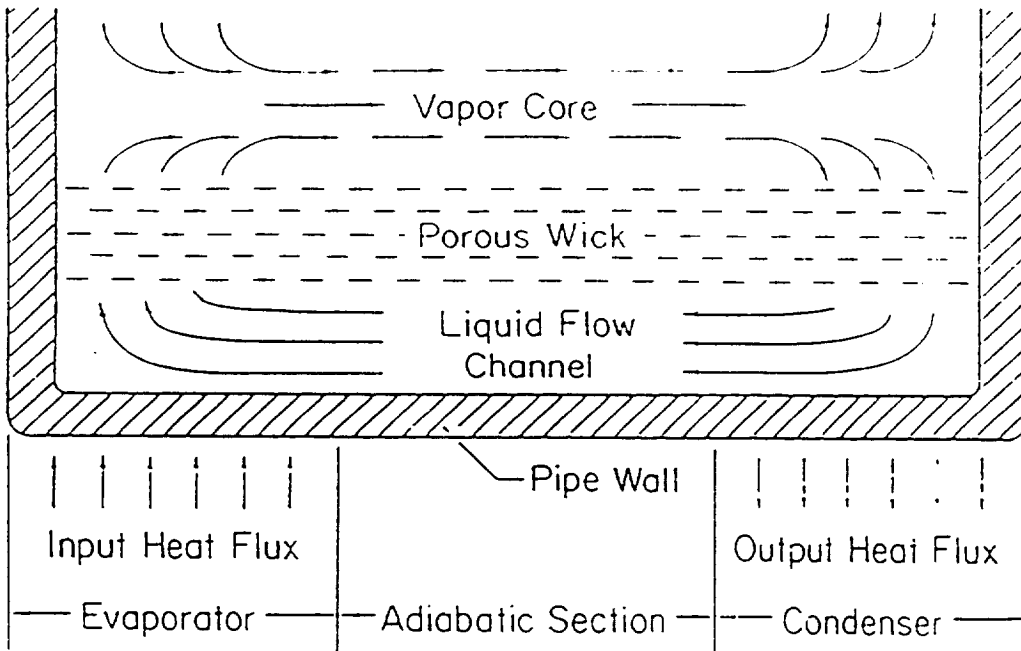
Figure 11: Flow Patterns in a Heat Pipe

6.1 GOVERNING EQUATIONS

The vapor flow in the heat pipe vapor core, shown in Fig. 11, is modeled as a channel flow shown in Fig. 12. The circular boundary of the channel is a thin porous medium which contains the liquid. The input heat flux to the evaporator and the temperature of the outer surface of the condenser are specified. The planar side walls are assumed adiabatic.

The equations governing the vapor flow are time dependent, viscous, compressible momentum, continuity and energy equations. An equation of state is used to relate pressure, density and temperature within the vapor core. These equations in axisymmetric coordinates (r,x) are

Figure 12: Vapor Core Model of a Heat Pipe

Continuity

$$\frac{\partial \rho}{\partial t} + \frac{\partial(\rho u)}{\partial x} + \frac{1}{r}\frac{\partial(\rho v r)}{\partial r} = 0 \tag{35}$$

x-Momentum

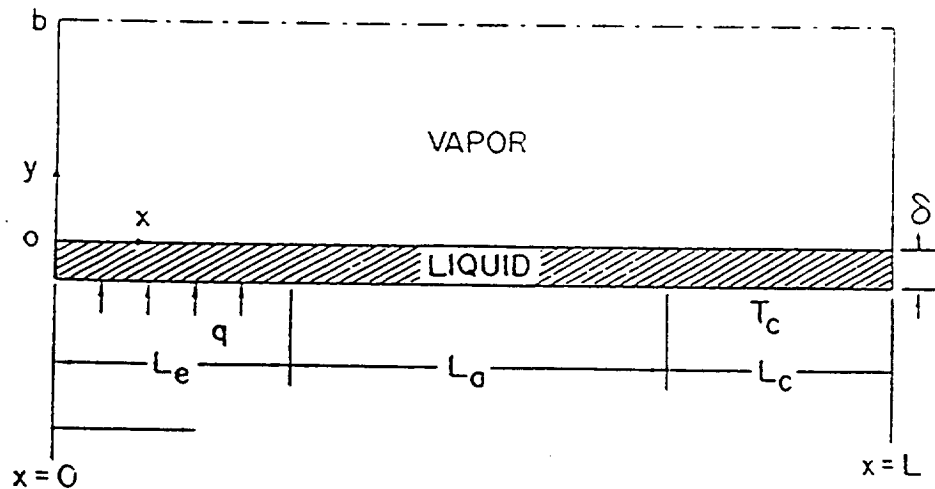$$\frac{\partial(\rho u)}{\partial t} + \frac{\partial(\rho uu)}{\partial x} + \frac{1}{r}\frac{\partial(\rho uvr)}{\partial r} = -\frac{\partial p}{\partial x} + \frac{\partial}{\partial x}\left(\mu\,\frac{\partial u}{\partial x}\right) + \frac{1}{r}\frac{\partial}{\partial r}\left(\mu r\,\frac{\partial u}{\partial r}\right)$$
$$+ \left\{\frac{\partial}{\partial x}\left(\mu\,\frac{\partial u}{\partial x}\right) + \frac{1}{r}\frac{\partial}{\partial r}\left(\mu r\,\frac{\partial v}{\partial x}\right) - \frac{2}{3}\frac{\partial}{\partial x}\left(\mu\,\frac{\partial u}{\partial x} + \frac{\mu}{r}\frac{\partial(rv)}{\partial r}\right)\right\} \tag{36}$$

r-Momentum

$$\frac{\partial(\rho v)}{\partial t} + \frac{\partial(\rho uv)}{\partial x} + \frac{1}{r}\frac{\partial(\rho vvr)}{\partial r} = -\frac{\partial p}{\partial r} + \frac{\partial}{\partial x}\left(\mu\,\frac{\partial v}{\partial x}\right) + \frac{1}{r}\frac{\partial}{\partial r}\left(\mu r\,\frac{\partial v}{\partial r}\right) +$$
$$\left\{\frac{\partial}{\partial x}\left(\mu\,\frac{\partial u}{\partial r}\right) + \frac{1}{r}\frac{\partial}{\partial r}\left(\mu r\,\frac{\partial v}{\partial r}\right) - \frac{2\mu v}{r^2} - \right. \tag{37}$$
$$\left. \frac{2}{3}\left(\mu - \frac{1}{r}\frac{\partial}{\partial r}\mu r\right)\left(\frac{\partial u}{\partial x} + \frac{1}{r}\frac{\partial vr}{\partial r}\right)\right\}$$

Energy

$$C_p\left[\frac{\partial(\rho T)}{\partial t} + \frac{\partial(\rho uT)}{\partial x} + \frac{1}{r}\frac{\partial(\rho vTr)}{\partial r}\right] = \frac{\partial p}{\partial t} + u\frac{\partial p}{\partial x} + v\frac{\partial p}{\partial r} + \frac{\partial}{\partial x}\left(k\frac{\partial T}{\partial x}\right) +$$
$$\frac{1}{r}\frac{\partial}{\partial r}\left(kr\frac{\partial T}{\partial r}\right) + \mu\left\{2\left(\frac{\partial u}{\partial x}\right)^2 + 2\left(\frac{\partial v}{\partial r}\right)^2 + 2\left(\frac{v}{r}\right)^2 + \left(\frac{\partial u}{\partial r} + \frac{\partial v}{\partial x}\right)^2\right\} \tag{38}$$

State

$$p = f(\rho, T) \tag{39}$$

6.1.1   *Boundary Conditions*

The boundaries of the vapor core are shown in Fig. 12. The nonslip condition for velocity and adiabatic condition for temperature are assumed on the side walls, i.e.,

@ $x = 0$ and $x = L$,

$$u = 0 \quad , \quad v = 0 \quad , \quad \frac{\partial T}{\partial x} = 0 \tag{40}$$

On the center line the symmetry condition implies,

@ $r = 0$,

$$\frac{\partial u}{\partial r} = 0 \quad , \quad v = 0 \quad , \quad \frac{\partial T}{\partial r} = 0 \tag{41}$$

The boundary conditions on the liquid-vapor interface are the challenging ones. The liquid flow is assumed in a porous medium with thickness δ, which is much smaller than the vapor core radius r_0. The axial velocity is assumed zero on this boundary. That is,

@ $r = r_0$,

$$u = 0 \tag{42}$$

In order to assign boundary conditions for the temperature and vertical velocity, the liquid-vapor interface is divided into three regions. In the evaporation

45

zone the input heat flux, q, is a given parameter and the input flow is approximated as,

@ $r = r_0$ and $0 < x \leq L_e$,

$$\rho v = \dot{m} \simeq \frac{q}{h_{fg}(T)} \tag{43}$$

In the above equation, h_{fg} is the heat of evaporization and conduction in the liquid layer is ignored. The temperature is assumed to be the saturation temperature of the liquid corresponding to the interface pressure. That is,

@ $r = r_0$ and $0 < x \leq L_e$,

$$T = T_{sat}(p) \tag{44}$$

In the adiabatic zone the boundary conditions are

@ $r = r_0$ and $L_e < x \leq (L_e + L_c)$,

$$v = 0 \ , \ \frac{\partial T}{\partial r} = 0 \tag{45}$$

In the condensation zone the temperature of the outer surface, T_c, is a given parameter. By equating the heat of evaporation to the heat conduction in the liquid layer, the outflow from this region is approximated as,

@ $r = r_0$ and $(L_e + L_c) < x \leq L$.

$$\rho v = \dot{m} \simeq - \frac{k_{eff}}{\delta} \left(\frac{T - T_c}{h_{fg}(T)} \right) \tag{46}$$

$$T = T_{sat}(p) \tag{47}$$

where, k_{eff} is the effective conductivity of the liquid layer and the temperature is assumed to be the saturation temperature corresponding to the pressure at the interface.

6.2 MIXED GALERKIN-FINITE DIFFERENCE METHOD

A mixed Galerkin-finite difference technique was used for the solution of the steady state equations, see Ref. [44]. In each partial differential equation the equation of state was substituted for the pressure, eliminating the pressure as a variable. This gave a system of four equations in four unknowns. Galerkin method was then applied, resulting in a pseudo two dimensional set of equations. Application of Galerkin method [45] involved choosing trial functions to represent each of the variables and substituting these in the equations. For the correct implementation of the Galerkin method, the trial functions chosen must have three requirements met.

1. They must be linearly independent.

2. They are part of a complete set of functions.

3. They must satisfy the boundary conditions exactly.

In this case the trial functions described the radial variation of the variables and exactly matched the boundary conditions in the radial direction. The trial functions used were as follows:

$$\rho(x,r,\tau) = \rho_w + \sum_n \hat{\rho}_n(x,\tau) f_1(r)$$

$$v(x,r,\tau) = f_3(r) V_w + \sum_n \hat{v}_n(x,\tau) f_2(r)$$

$$u(x,r,\tau) = \sum_n \hat{u}_n(x,\tau) f_1(r)$$

$$T(x,r,\tau) = T_w + \sum_n \hat{T}_n(x,\tau) f_1(r)$$

where the basis functions $f_1(r)$, $f_2(r)$ and $f_3(r)$ are defined as:

$$f_1(r) = \cos\left((2n-1)\frac{\pi r}{2R_1}\right)$$

$$f_2(r) = \frac{r}{R_1} \sin\left(n\pi \frac{r}{R_1}\right)$$

$$f_3(r) = \left(\frac{r}{R_1}\right)^2$$

Note that the functions f_n are chosen to satisfy the radial boundary conditions. Three of the trial functions include a term in front of the summation of coefficients. This additional term, denoted with the subscript w, represents the known value of the variable at the wall, where $r = R_1$. At the wall the radial functionality of the trial function becomes zero, so that the variable is completely defined by the wall term. A function of radius, f_3 was included with the wall term for radial velocity. This was to insure that the radial velocity went to zero at the centerline.

48

Substitution of the trial functions into the differential equations creates the residual, R. Finally, weighting functions, F_w, are chosen for each equation and the inner product of each residual and its weighting function is calculated. Weighting functions chosen for this analysis are given below:

Mass

$$F_{w1} = f_1(r) = \cos\left((2k - 1)\frac{\pi r}{2R_1}\right)$$

X-Momentum

$$F_{w2} = f_1(r) = \cos\left((2k - 1)\frac{\pi r}{2R_1}\right)$$

R-Momentum

$$F_{w3} = f_2(r) = \frac{r}{R_1}\sin\left(k\pi\frac{r}{R_1}\right)$$

Energy

$$F_{w4} = f_1(r) = \cos\left((2k - 1)\frac{\pi r}{2R_1}\right)$$

Ideally the weighting functions should be orthogonal with the trial functions, but in the problem at hand that was not possible. Here, we define the inner product as:

$$(R, F_w) = \int_r F_w R r dr$$

where R is the residual, F_w is the weighting function and the product is integrated over the cross section. These calculations are carried out in detail in Reference 44. A set of nonlinear differential equations (with respect to the axial direction) result that can be solved using any of several methods.

49

6.2.1 Results

Although more promising than the finite difference method described in section 6.3, a number of difficulties were encountered and the press of time constraints did not allow them to be overcome. It is still our view that the mixed finite difference-Galerkin method or full Galerkin method is the only method that will yield the needed computational speed. The following paragraphs document some of our struggles to "make it work".

Converged results from the analysis have not provided any more insight into heat pipe vapor dynamics than was previously known. Several types of vapor flow in the heat pipe have been input to the code to see if accurate and meaningful results could be obtained. Solutions used for checkout corresponded to a 'zero solution', a stagnant tube, fully developed pipe flow and finally the heat pipe operating mode.

Corresponding to a 'zero solution' are Dirichlet boundary conditions of zero for density, radial velocity and temperature at the wall. The corresponding internal coefficients for the Galerkin representation should then be calculated to be zero as well. A stagnant tube corresponds to the geometry of a sealed tube at constant, uniform temperature and density. Hence, values for density and temperature through the pipe are equal to the wall value. Coefficients for the Galerkin representation of these variables should be zero. Consistent with the stagnant tube, all vapor velocities should also be zero.

Determining boundary conditions consistent with flow in a pipe required that the program be modified slightly. Modifications were primarily in regards to the axial boundary conditions on axial velocity. Previous conditions stated

that all velocity components at $x = 0$ and $x = L$ were zero due to the solid boundary at the ends. For pipe flow, it was intended to model a small section cut from a long, straight pipe. Thus, in the model, a fully developed for the axial velocity could be used at $x = 0$, and at first was also used at $x = L$. However, the conditions proved to be inconsistent because vapor flow was being forced through a tube, but with constant density and temperature there was no pressure drop. A remedy to this problem was to use a Neumann boundary condition at the right end of the pipe, $\frac{du}{dx} = 0$ at $x = L$, and set either density or temperature to be decreasing axially from $x = 0$ to $x = L$, with a linear profile. In this manner, the actual value of the axial velocity was not set, so it could adjust to the changing pressure along the pipe.

Finally the heat pipe operation was implemented. Under this mode of operation, the axial velocity is set equal to zero at all the boundaries while the radial velocity is set equal to zero at the two ends, $x = 0$ and $x = L$. In the evaporator the radial velocity is set equal to a finite negative value at the wall, and to a finite positive value at the wall in the condenser. At the wall in the adiabatic section a zero radial velocity was assumed corresponding to no mass evaporation or condensation. Because this was a steady state analysis, the total mass flow in the evaporator was equal to the total mass flow in the condenser. Density at the wall was held constant for this try and the wall temperature was given a profile which decreased axially toward the condenser. This was consistent with a heat pipe operating under a steady heat flux and allowed for decreasing pressure in the direction of flow.

51

An instance may be documented in which the current equation set will fail as it is. For the 'zero solution', i.e., all boundary conditions are zero, so the coefficients of the Galerkin trial functions are also zero, the equation vector on the right hand side of the iteration equation is indeed zero, but for a solution, the Jacobian must be calculated and non-zero terms must be obtained. Jacobian elements for all terms on the diagonal may be determined for the energy equation and the two momentum equations. However, the conservation of mass equation will have no non-zero terms, because all Jacobian derivatives of this equation still have a coefficient of wall term which is zero.

The code was run for the 'zero solution'. Two sets of initial conditions were used for the Galerkin coefficients. As a first guess the coefficients were initially set to zero. This proved to exactly solve the set of equations, as only one iteration was used and the zero solution was returned. Then the initial guess for the coefficients was set to 0.0005. With this guess the program required two iterations to converge with a maximum iteration error of $6.5 \cdot 10^{-5}$ on the temperature. In this case, however, the coefficients were non-zero, with the largest magnitude being $5.0 \cdot 10^{-4}$ for the density, $3.1 \cdot 10^{-8}$ for the axial velocity, $1.0 \cdot 10^{-8}$ for the radial velocity and $8.4 \cdot 10^{-4}$ for the temperature.

Solution for a stagnant tube required 21 iterations from an initial guess of 0.0005. The maximum iteration error was $9.6 \cdot 10^{-5}$. Again, this obtained for the temperature. The maximum magnitude of the converged values was $1.5 \cdot 10^{-4}$ for the density, $2.5 \cdot 10^{-7}$ for the axial velocity, $1.7 \cdot 10^{-6}$ for the radial velocity and $4.7 \cdot 10^{-4}$ for the temperature. For comparison, wall values

for density and temperature were 1.0 and 3.0, respectively, and the calculated, normalized sonic velocity was 2.8.

These two cases are the only ones the code would definitely converge on. They were obtained on an eleven grid matrix with a spacing of 0.01. Following these two cases, the pipe flow configuration was attempted. Using the same grid network with Dirichlet boundary conditions at $x = 0$ and Neumann conditions at $x = L$ for the axial velocity, no solution was obtained. In this configuration only the axial velocity coefficients were updated. Radial velocity was everywhere set equal to zero as were the coefficients of the density and temperature. Hence, the density and temperature were axially and radially constant. Iterations on the axial velocity diverged slowly at first, then rapidly around the 18th iteration.

An additional pipe flow case was considered in which both axial and radial velocities were updated at each iteration. Using the same grid network the solution diverged again, this time after 32 iterations.

Finally, the code was run for the heat pipe configuration, using constant density and injected vapor velocity of -0.01. Condensing vapor in the condenser was given a velocity of +0.01. Wall temperature varied axially from 3.2 in the evaporator to 2.8 in the condenser. Updating all variables and using an initial guess of of 0.0 for all coefficients, the solutions diverged after 9 iterations. A damping factor of 0.77 was included. Here, the calculated coefficients after the 9th iteration displayed a noticeable amount of cell Reynolds number problems. To try and correct the problem, the grid spacing was cut in

half. Using the same boundary conditions and the initial guess, the solution appeared to be oscillating after 40 iterations and failed to converge.

In general, results from using the code for the heat pipe configuration have all failed. One problem evident from the output has been a cell Reynolds problem. However, increasing the number of nodes, although permitting more iterations without diverging, still does not allow consistent, meaningful results to be calculated.

Although grid spacing and the resulting cell Reynolds problems may have been a problem, it does not appear to be the only one. Some equation formulations have instabilities within them and one way to arrive at consistent solutions is by including damping. A method of upwind differencing was utilized. This too seemed to make little difference to the computed solutions.

Completeness of the basis functions used to represent the variables in the Galerkin expansion is another point in question. For the cylindrical coordinate system it probably would have been better to use Bessel functions as the basis functions.

It looks like the boundary conditions themselves may have caused problem which the mixed Galerkin-finite difference method does not handle well. Boundary conditions on the radial velocity are sharply discontinuous, with the velocity being negative in the evaporator, zero in the adiabatic region and positive in the condenser. Changes between the regions occur as sharp jumps. Trial functions chosen to represent this variable could not satisfy these conditions with a single basis function alone, but relied on the constant term added to this basis function to match the requirements completely. However, con-

stant term still poses sharp discontinuities in the axial direction. It may be that the failure of the basis functions alone to satisfy the boundary conditions causes the Galerkin method to not converge to a solution. It appears the Galerkin method is not well suited to handle the boundary conditions associated with this type of a compressible flow problem.

In conclusion, there are several aspects of this work that could have been valuable, had a solution be obtained. The basic problem studied, compressible heat pipe vapor dynamics in two dimensions, is a topic of current interest in many communities around the world and a capability of detailed analysis is needed. Secondly, the method of solution, mixed Galerkin-finite difference method, is not one that is often applied to a compressible flow problem. Successful application of this method as well as the direct solution of the steady state equations could have been a contribution of interest to the field of numerical fluid mechanics.

6.3 PROPOSED SOLUTION METHOD

Equations (35) to (39) are five equations in five unknowns, namely, ρ , u , v , T and p . The boundary conditions associated with these equations are Eqs. (40) to (47). The boundary conditions on the vapor-liquid interface depend on the interface pressure and pressure is not available on the boundaries. However, in the numerical method described below, the pressure does not need to be specified on the boundaries. Then, after completion of the calculations, an interpolation method is used to determine the pressure on the boundaries.
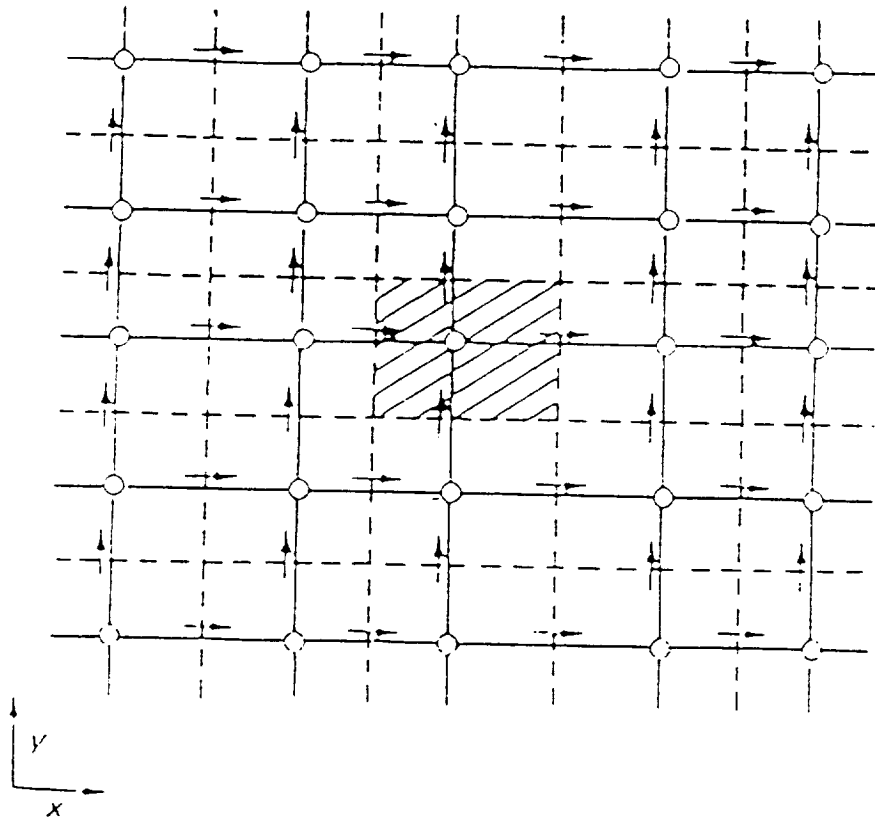
— locations for u, ⊦ locations for v,
o locations for p, T and p

Figure 13: Staggered Grid

The numerical scheme used here is based on the SIMPLE method described by Patankar [43]. In this method all the variables are not evaluated on the same point, but a staggered grid, as shown in Fig. 13, is used. By choosing control volumes which have the cell centers at their center, the velocity components are evaluated for the points that lie on the faces of the control volumes. The locations for u and v are shown by short arrows in the Figure. The other dependent variables, namely, p , T and p , are calculated for the cell centers shown by small circles. The boundaries do not lie on the cell centers.

The algorithm for calculations is the following :

The system pressure is assumed to be composed of two parts

$$p(x,r,t) = \bar{p}(t) + \tilde{p}(x,r,t) \tag{48}$$

where $\bar{p}(t)$ is the space averaged system pressure whereas $\tilde{p}(x,r,t)$ includes the space variation of the pressure. Assuming a pressure distribution, the momentum equations (Eqs. (36),(37)) are solve for velocity components u and v at a time step. Then using the continuity equation and density ρ from the last iteration on temperature, the pressure is corrected to be used again in momentum equations. Upon accomplishing these iterations, the velocity field and $\tilde{p}(x,r,t)$ will be found.

Using the velocity field, the energy equation (Eq. (38)) is then solved for temperature. In order to calculate density from the equation of state, and to evaluate the boundary conditions, we need the absolute value of the pressure. Global mass balance is used to calculate the absolute pressure. The total mass, for an ideal gas, m , is related to the pressure by

$$m = \int_V \rho dV = \int_V \frac{p}{RT} dV \tag{49}$$

where V is the volume. The increase in the total mass in one time step is

$$m(t + \Delta t) - m(t) = (\dot{m}_{in} - \dot{m}_{out})\Delta t \tag{50}$$

where $\dot{m}_{in}$ and $\dot{m}_{out}$ are the input and output mass fluxes, respectively, and are calculated from the boundary conditions. Equations (49) and (50) are combined to yield

$$(\dot{m}_{in} - \dot{m}_{out})\Delta t = \int_V \left(\frac{p|_{t+\Delta t}}{RT|_{t+\Delta t}} - \frac{p|_t}{RT|_t} \right) dV \qquad (51)$$

Thus Eq. (51) is used to evaluate the absolute pressure of the system. For a real gas, using an equation of state, the above procedure is followed to calculate the total pressure.

6.4 PRELIMINARY RESULTS

The computational procedure described above was implemented for a two dimensional time dependent compressible flow with the same type of heat pipe boundary conditions as those mentioned above. The computations were performed for several evaporator heat fluxes with water as the working fluid and pipe dimensions of $r_0 = 2.5 \ cm$ and $L = 3r_0$. The computational grid spacings were $\Delta x / r_0 = 0.1$ and $\Delta y / r_0 = 0.05$. The temperature and pressure variations, and consequently, the density variation, were found to be quite small inside the pipe. This is expected of systems in which condensation takes place without a non-condensible gas.

The steady state results are shown in Figs. 14, 15 and 16. The steady state was assumed to be reached when the relative change of all variables (error

58
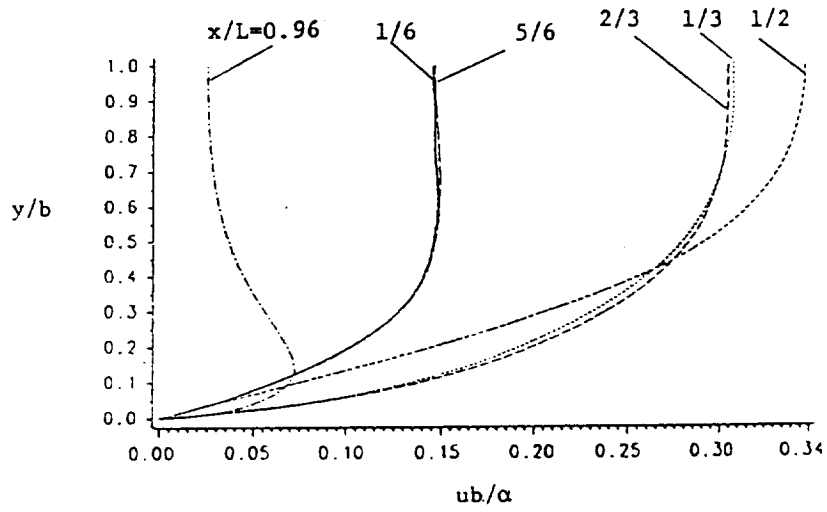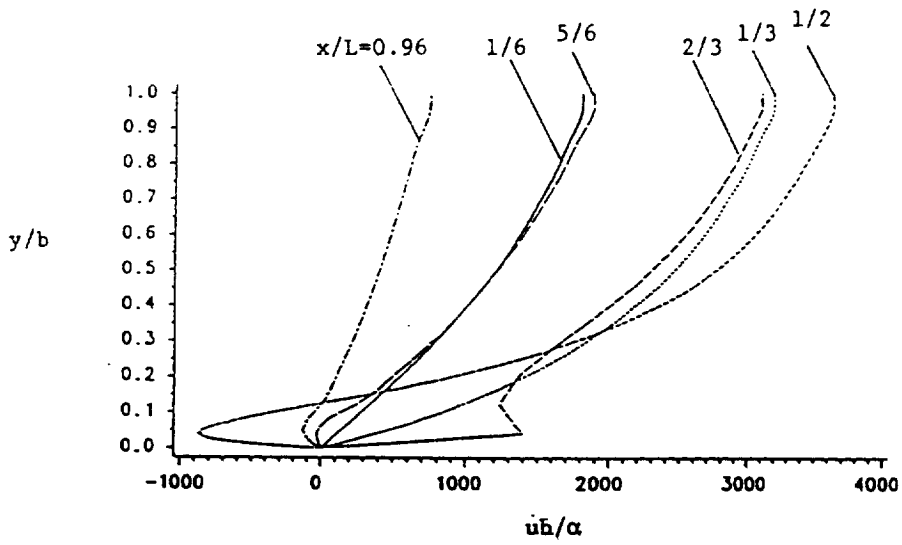
Figure 14: Axial Velocity Profiles
(a) low input heat flux (Re = 1),
(b) high input heat flux (Re = 1000).
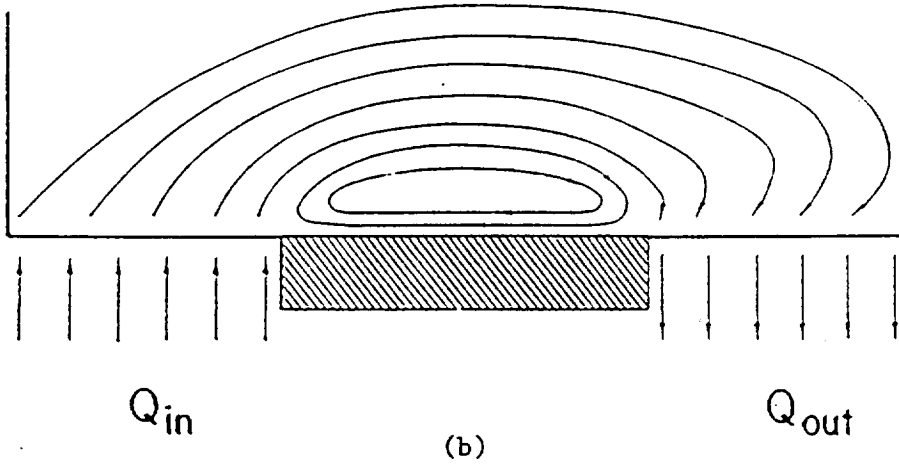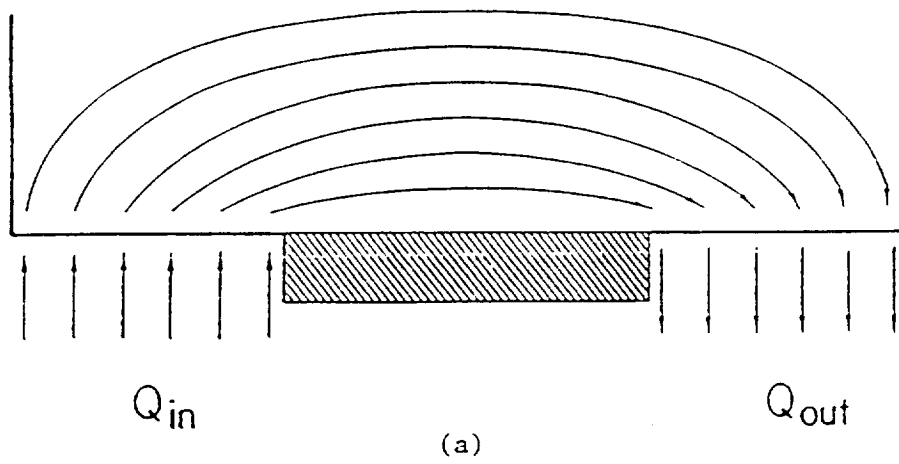
Figure 15: Schematic of Flow Streamlines
(a) low input heat flux, (b) high input heat flux.

norm) within a time step was less than 0.5%. Figures 14 show the axial veloc-
ity profiles at different axial cross sections along the pipe, for low input heat
flux, Fig. 14(a), and for high input heat flux, Fig. 14(b). The flow stream lines
for these two cases are shown schematically in Fig. 15.
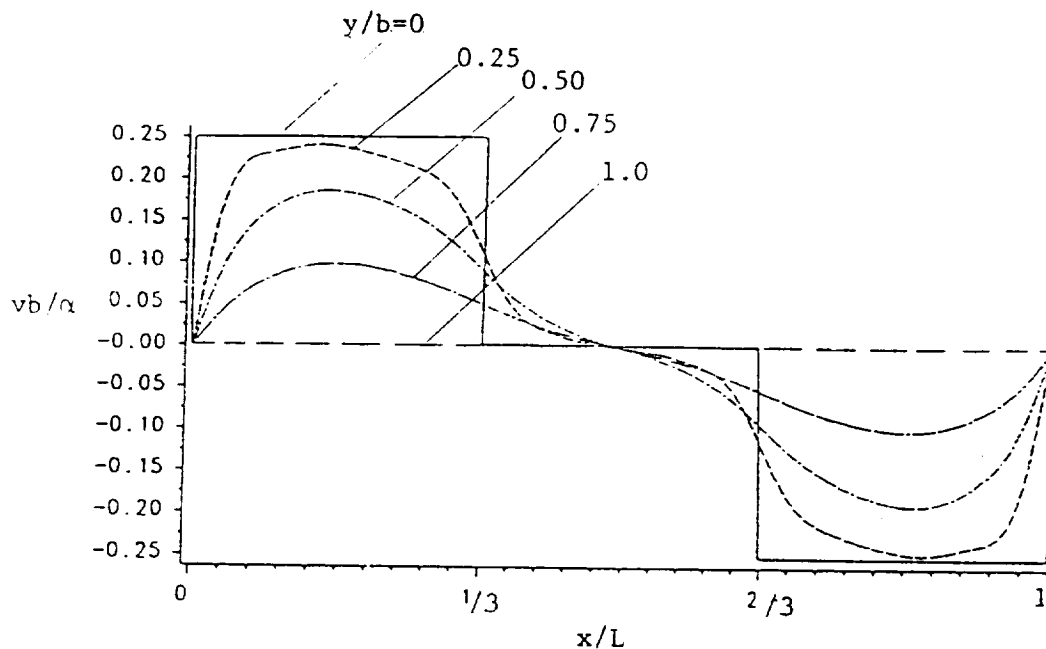
Figure 16: Vertical Velocity Profiles

When the input heat flux is relatively low, the evaporation rate is low and the vapor flows smoothly towards the condensation region (Figs. 14(a) and 15(a)). However, with high input heat flux the evaporation rate is high, the vapor is ejected with a high momentum from the evaporator and under steady state conditions, condenses at a high rate at the condenser. The high momentum flow at two ends of the adiabatic section causes a circulation flow in this region. That is, on the adiabatic surface there is a reverse flow. In addition, in the condensation region the high momentum vapor flow impacts the rigid end wall, returns and then condenses in the liquid region. This return flow is

61

x/L=0.5

y/b

ub/α
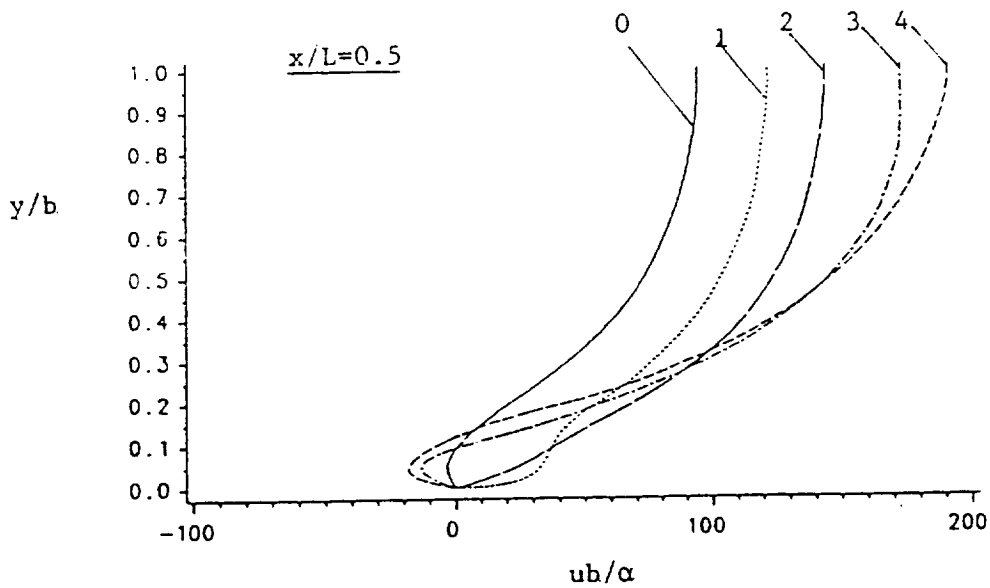
0- initial profile ($\tau = 0$),
1- $\tau = 10^{-4}$,
2- $\tau = 2.5 \cdot 10^{-3}$,
3- $\tau = 10^{-2}$,
4- steady state ($\tau = 2.5 \cdot 10^{-2}$)
where $\tau = t\alpha/b^2$.

Figure 17: Axial Velocity Profile at Different Time Steps

shown in Figs. 14(b) and 15(b). The vertical velocity profiles for different vertical cross sections are shown in Fig 16. The flow is clearly two dimensional.

Transient behavior of vapor flow was studied by using a steady state solution as the initial conditions for different input parameters. As an example, Fig. 17 shows the axial velocity profiles at the middle of the pipe, $x/L = 0.5$, at different time steps. Curve 0 on this Figure is the steady state solution for $Re = 100$, where Reynolds number is defined as

$$Re = \frac{\dot{m}_{in} \, r_0}{\mu}$$

and $\dot{m}_{in}$ is the input mass flux. Curves 1 to 4 show this velocity profile at different time steps after a sudden increase in input heat flux for $Re = 200$. At the outset, the increase in input heat flux overcomes the reverse flow, see curve 1. As the velocity profile develops with time, the steady state profile, curve 4, shows a higher reverse flow at the liquid-vapor interface.

6.5 PROPOSED ANALYSIS

The dynamic behavior of vapor flow in heat pipes is studied for transient operations. The above analysis needs to be modified as follows:

1. The existing computer code is able to handle two dimensional transient vapor flow in Cartesian coordinates. The code must be modified to axisymmetric coordinates for analyzing circular heat pipes.

2. Interesting phenomena have been detected in the adiabatic and condensation regions. In these regions high input heat flux may cause a reverse flow. The reverse flow results in negative shear force on the wick structure. A parametric study is needed to explore the reverse flow versus design parameters like the evaporator, condenser, adiabatic and total length of the heat pipe for different input heat fluxes and condenser temperatures.

3. Effects of the presence of a non-condensible gas in the vapor core on the condensation rate and the heat pipe operation will be also investigated.

4. Many heat pipe applications result in irregular geometries. Grid generation techniques need to be incorporated into the code to accommodate them.

5. The vapor flow has been dealt with using simplified boundary conditions. The liquid phase model, see Chapter VII, needs to be used to generate the proper boundary conditions.

Chapter VII

THEORETICAL MODEL OF THE LIQUID PHASE

As previously discussed, most research in heat pipe dynamics has focused on the startup transient. An experimental investigation has also been performed for the shutdown transient. Only modest efforts have been expended to date that consider operational transients. These efforts generally address two issues: the capability to achieve nominal operation under specified conditions, and the resulting axial temperature distribution. The processes are assumed to occur quasisteadily such that time dependent characteristics are not considered. Despite these research efforts, a comprehensive analytical model does not exist that captures the physical processes while being economical enough for required computations.

The objective of this part of the study is to develop an analytical model of the liquid phase of a high temperature heat pipe. The model is intended to be coupled to a vapor phase model for the complete solution of the heat pipe problem. The mathematical equations are formulated consistent with physical processes while allowing a computationally efficient solution. The model simulates time dependent characteristics of concern to the liquid phase, including: input, phase change, and output heat fluxes, liquid temperatures, container temperatures, liquid velocities, and liquid pressures.

This research considers requirements for high temperature, high thermal flux operation with heat transport over long distances and small temperature drops. These requirements indicate the need for a heat pipe with a high performance composite wick. A composite wick consists of small pores at the liquid-vapor interface and large pores in the direction of bulk liquid flow. Recall that the maximum capillary pumping capability is limited by the largest capillary surface at the liquid-vapor interface as shown by Eq. (4). The small pores at the liquid-vapor interface establish a high capillary pumping capability that drives the circulation of working fluid. The larger pores in the direction of flow provide a low resistance flow path for the liquid.

The heat pipe selected for this study uses an annular wick configuration as shown in Fig. 18. The annular wick is an excellent configuration for liquid metals, is popular for experimental work, and involves geometry easily modeled in cylindrical coordinates [27,28]. The wick configuration consists of several layers of fine pore screen pressed together and concentrically installed in the pipe to form an annular flow channel as shown in Fig. 19. The annulus forms the low resistance flow channel while the fine pore screen tube forms the high pumping capability boundary between the liquid and vapor regions.

The capillary wick introduces some analytical although not conceptual difficulty. A thin screen tube consisting of several layers of pressed screen forms a tortuous flow channel with no slip conditions on the surface of the screen wires. Explicit analysis of the flow including consideration of the large number of wire surfaces involved would be difficult if at all practical considering the goal of performing transient analysis. A macroscopic approach such as
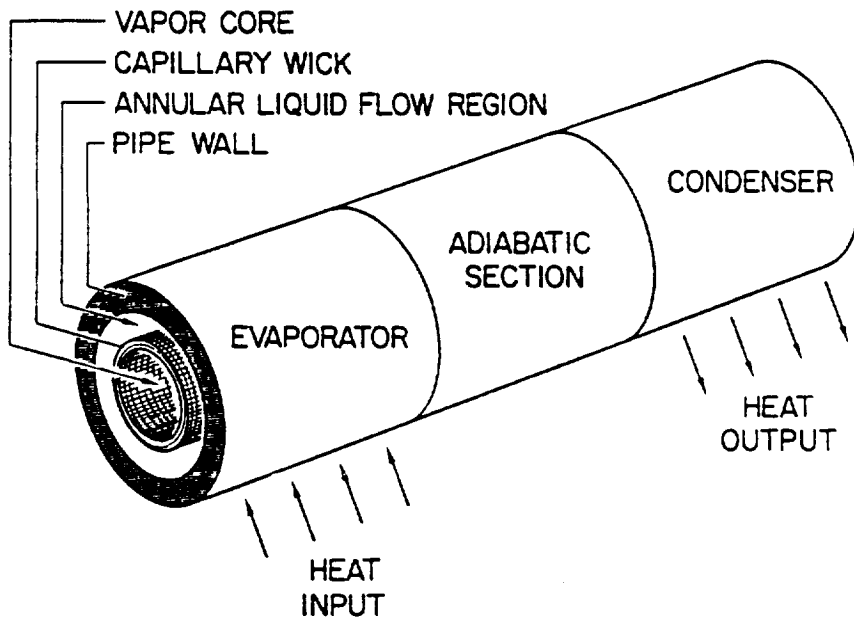
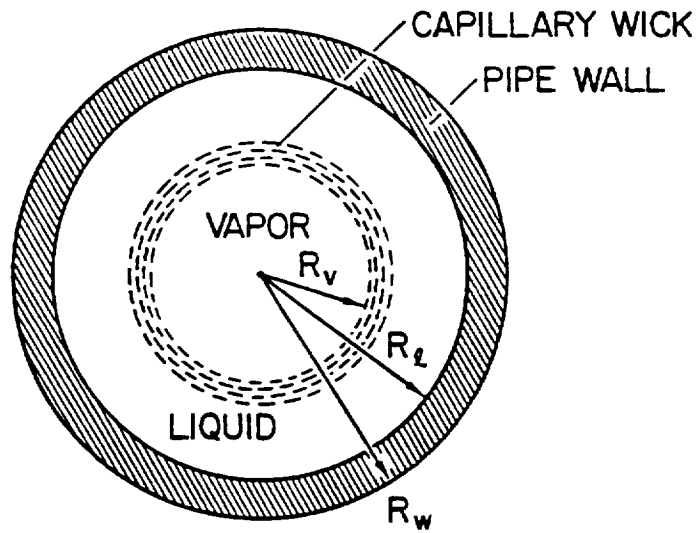Figure 18: Heat Pipe with High Performance Composite Annular Wick

Figure 19: Cross Section of High Performance Annular Wick Configuration

Darcy's Law for flow in a porous medium could be used to alleviate the complexity. However the axial flow in the pressed screen is expected to be small relative to axial flow in the open annular channel. Indeed, the very purpose of the annular composite wick configuration is to provide a low resistance flow channel in the annulus for circulation of liquid. The screen tube is used only to provide a fine capillary surface at the liquid-vapor interface. The screen tube can then be approximated as a single layer of screen with a characteristic pore size. Flow normal to the screen is restricted by a characteristic specified porosity, while tangential flow is governed by alternating free slip and no slip conditions. The free slip condition provides the tangential shear communication between the liquid and vapor phases. The wick is approximated then as an infinitesimally thin porous surface.

7.1 THE LIQUID PHASE MATHEMATICAL FORMULATION

7.1.1 *Assumptions*

The governing equations to be presented below will be reduced by recognizing unique characteristics of the system to be analyzed. The system is assumed to operate in an essentially gravity free environment. Other body forces such as those due to translational and rotational acceleration will also be neglected.

The heat pipe is assumed to be installed with azimuthal symmetry in the particular application. The thermal energy source adds heat uniformly around

68

the evaporator circumference while the heat sink extracts heat uniformly around the condenser circumference. The resulting uniform conditions in the azimuthal direction imply there are no velocity components or gradients in the azimuthal direction.

Liquid flow in a heat pipe wick is generally low speed, laminar, and incompressible. Since the liquid flow field is relatively simple and the cross-stream dimension of the liquid region is much smaller than the streamwise dimension, the cross-stream (i.e., radial) pressure gradient is assumed to be negligible. Also since the flow is low speed and incompressible, viscous energy dissipation can be neglected.

In summary, the assumptions to be used for reducing the governing equations are:

1. Negligible body forces: $f_r = f_x = 0$

2. Azimuthal symmetry

   a. No azimuthal flow: $w = 0$

   b. No azimuthal gradients: $\dfrac{\partial \cdot}{\partial \phi} = 0$

3. Negligible radial pressure gradient: $\dfrac{\partial P}{\partial r} = 0$

4. Negligible viscous dissipation

5. Incompressible liquid: $\dfrac{\partial \rho_l}{\partial P} = 0$

6. Laminar liquid flow

Thermophysical properties are considered to be uniform functions evaluated at a reference temperature. The reference temperature is assumed to change slowly with time such that properties can be treated as constants in the governing equations.

69

7.1.2 Governing Equations

Temperatures of the heat pipe container and the temperatures, pressures, and velocities of the liquid phase are required to describe the dynamic behavior of the liquid phase of a high temperature heat pipe under transient operating conditions. The governing equations describing the behavior of these parameters consist of the conservation of mass, momentum, and energy.

The full condition governing conservation of mass of an incompressible fluid is

$$\frac{\partial u}{\partial x} + \frac{\partial v}{\partial r} + \frac{1}{r}\frac{\partial w}{\partial \phi} + \frac{v}{r} = 0 \tag{52}$$

where u is the velocity in the axial (x) direction, v is the radial (r) velocity, and w is the azimuthal direction (ϕ) velocity. Imposing the assumption of azimuthal symmetry reduces Eq. (52) to the familiar two dimensional form

$$\frac{\partial u}{\partial x} + \frac{\partial v}{\partial r} + \frac{v}{r} = 0 \tag{53}$$

Full conservation of radial momentum for an incompressible fluid with constant properties is given by

$$\frac{\partial v}{\partial t} + \frac{\partial uv}{\partial x} + \frac{\partial v^2}{\partial r} + \frac{1}{r}\frac{\partial wv}{\partial \phi} - \frac{w^2}{r} + \frac{v^2}{r} =$$
$$-\frac{1}{\rho}\frac{\partial P}{\partial r} + v\left(\frac{\partial^2 v}{\partial x^2} + \frac{\partial^2 v}{\partial r^2} + \frac{1}{r^2}\frac{\partial^2 v}{\partial \phi^2} + \frac{1}{r}\frac{\partial v}{\partial r} - \frac{2}{r^2}\frac{\partial w}{\partial \phi} - \frac{v}{r^2}\right) + f_r \tag{54}$$

70

where t is the time, ρ is density, P is pressure, and ν is kinematic viscosity. By assuming negligible radial pressure gradient, the conservation of radial momentum equation is replaced by

$$\frac{\partial P}{\partial r} = 0 \tag{55}$$

Under this approximation the radial momentum equation is not used to define liquid dynamics so that pressure is determined from the continuity equation and the axial momentum equation.

Conservation of axial momentum for an incompressible fluid with constant properties is given by

$$\frac{\partial u}{\partial t} + \frac{\partial u^2}{\partial x} + \frac{\partial uv}{\partial r} + \frac{1}{r}\frac{\partial uw}{\partial \phi} + \frac{uv}{r} =$$
$$-\frac{1}{\rho}\frac{\partial P}{\partial x} + \nu\left(\frac{\partial^2 u}{\partial x^2} + \frac{\partial^2 u}{\partial r^2} + \frac{1}{r^2}\frac{\partial^2 u}{\partial \phi^2} + \frac{1}{r}\frac{\partial u}{\partial r}\right) + f_x \tag{56}$$

Assuming negligible body forces, azimuthal symmetry and no radial pressure gradient reduces Eq. (56) to

$$\frac{\partial u}{\partial t} + \frac{\partial u^2}{\partial x} + \frac{\partial uv}{\partial r} + \frac{uv}{r} = -\frac{1}{\rho}\frac{dP}{dx} + \nu\left(\frac{\partial^2 u}{\partial x^2} + \frac{\partial^2 u}{\partial r^2} + \frac{1}{r}\frac{\partial u}{\partial r}\right) \tag{57}$$

Full conservation of energy for an incompressible, constant property fluid is given by

$$\rho c_v \left[\frac{\partial T}{\partial t} + u\frac{\partial T}{\partial x} + v\frac{\partial T}{\partial r} + \frac{w}{r}\frac{\partial T}{\partial \phi} \right] =$$

$$k\nabla^2 T + 2\mu \left\{ \left(\frac{\partial u}{\partial x}\right)^2 + \left(\frac{\partial v}{\partial r}\right)^2 + \left[\frac{1}{r}\left(\frac{\partial w}{\partial \phi} + v\right)\right]^2 \right\} + \qquad (58)$$

$$\mu \left\{ \left[\frac{\partial v}{\partial x} + \frac{\partial u}{\partial r}\right]^2 + \left[\frac{\partial w}{\partial x} + \frac{1}{r}\frac{\partial u}{\partial \phi}\right]^2 + \left[\frac{1}{r}\frac{\partial v}{\partial \phi} + r\frac{\partial}{\partial r}\left(\frac{w}{r}\right)\right]^2 \right\}$$

Neglecting viscous dissipation and assuming azimuthal symmetry results in

$$\frac{\partial T}{\partial t} + u\frac{\partial T}{\partial x} + v\frac{\partial T}{\partial r} = \alpha\left(\frac{\partial^2 T}{\partial x^2} + \frac{\partial^2 T}{\partial r^2} + \frac{1}{r}\frac{\partial T}{\partial r}\right) \qquad (59)$$

The conservation of mass and momentum equations are solved subject to the boundary conditions using an integral method, whereas the conservation of energy equation is solved using the finite difference method. The computational implementation of the solution approach will be discussed in section 7.3.

7.1.3 Boundary Conditions

The heat pipe boundary conditions can be considered as either external or internal. The external conditions refer to the communication of the heat pipe external surface with the surrounding environment. The internal conditions are of two types: fluid-solid and fluid-fluid. The fluid-solid conditions refer to the interaction between the liquid and either the pipe internal surface or the wick. Fluid-fluid conditions govern the interaction between the liquid and vapor phases.

The heat pipe external boundary can be divided into three convenient regions as shown in Fig. 18. The evaporator region absorbs heat from the envi-

72

ronment, the adiabatic region exchanges no heat with the environment, and the condenser rejects heat to the environment. The evaporator surface is assumed to be exposed to a known surface heat flux condition, while the condenser exchanges heat through radiation[1] to a sink of known temperature [26]. The conditions on the pipe external wall are then

AXIAL RANGE	RADIAL RANGE	CONDITION
$0 \leq x \leq L_e$	$r = R_w$	$-k\dfrac{\partial T}{\partial r} = q_{in}(x, t)$
$L_e < x < L_e + L_a$	$r = R_w$	$\dfrac{\partial T}{\partial r} = 0$
$L_e + L_a \leq x \leq L$	$r = R_w$	$-k\dfrac{\partial T}{\partial r} = q_{rad}$

where q_{in} is specified and q_{rad} is to be determined from $q_{rad} = \varepsilon\sigma(T_w^4 - T_e^4)$ assuming environmental sink temperature T_e is known.

---

[1] The condenser could generally exchange heat with the environment through conduction, radiation, and convection. However, the study of radiation loaded elements is of current research interest for space based applications [25].

Long heat pipes with large evaporator and condenser circumferential sur-
face areas relative to the surface area of pipe endcaps will normally have neg-
ligible effects due to conduction in the end caps. With this assumption, the
boundary conditions are:

AXIAL RANGE	RADIAL RANGE	CONDITION
$x = 0$	$R_l \leq r \leq R_w$	$\dfrac{\partial T}{\partial x} = 0$
$x = L$	$R_l \leq r \leq R_w$	$\dfrac{\partial T}{\partial x} = 0$

Solid-fluid surfaces correspond to the heat pipe container internal wall interface with the working fluid, and the capillary wick interface with the fluid. The pipe wall conditions are no slip and matching temperature gradient. The conditions are:

AXIAL RANGE	RADIAL RANGE	CONDITION
$x = 0$	$R_v \leq r \leq R_l$	$u = 0$
		$v = 0$
		$\dfrac{\partial T_l}{\partial x} = 0$
$x = L$	$R_v \leq r \leq R_l$	$u = 0$
		$v = 0$
		$\dfrac{\partial T_l}{\partial x} = 0$
$0 \leq x \leq L$	$r = R_l$	$u = 0$
		$v = 0$
		$k_l \dfrac{\partial T_l}{\partial r} = k_w \dfrac{\partial T_w}{\partial r}$
$0 \leq x \leq L$	$r = R_v$	

The liquid-vapor interface of the heat pipe is the most difficult feature to analyze. The interface serves as the medium for communication between the

75

liquid and vapor along the entire axial length of the pipe. The flow characteristics are distinctly different between the respective liquid and vapor sides of the interface. The interface is subjected to physical phenomena through the action of surface tension that is generally not considered in the liquid or vapor flow fields.[2] The general liquid-vapor interface conditions are as the following:

Kinematic Surface Condition

$$\vec{U}_{lv} = 0 \tag{60}$$

where $\vec{U}_{lv}$ is the velocity of the liquid-vapor interface surface.

Conservation of Mass

$$\rho_v V_{0v} = \rho_l V_{0l} \tag{61}$$

where V_{0v} is the vapor radial phase change velocity and V_{0l} is the liquid radial phase change velocity. In future uses, V_0 will refer to the liquid phase change velocity unless for clarity V_{0l} is used.

Continuity of Tangential Stress

The tangential stress condition provides an important coupling relation between the liquid and vapor phases. Since the vapor phase solution is not included in this study, as a first approximation the vapor tangential shear stress will be neglected and replaced with the axial velocity no slip condition

---

[2] The vapor and liquid regions are each assumed to be a single phase such that multi-phase phenomena in these bulk flow regions are not considered. Entrainment of liquid by shearing action of the vapor, condensation in the bulk vapor, and vapor bubble formation in the liquid are common examples of departures from the single phase assumption. These phenomena are outside the scope of the present analysis.

$$u_0 = 0 \tag{62}$$

Continuity of Normal Stress

$$P_v - P_l + \rho_v V_{0v}(V_{0v} - V_{0l}) + 2\left[\mu_l \frac{\partial v_l}{\partial r} - \mu_v \frac{\partial v_v}{\partial r}\right] = \sigma\left(\frac{1}{R_1} + \frac{1}{R_2}\right) \tag{63}$$

Continuity of Thermal Flux

$$C_w \rho_v V_{0v} h_{fg} = -k_l \frac{\partial T_l}{\partial r} \tag{64}$$

where

$$C_w = \left[\frac{D_p}{D_p + D_w}\right]^2$$

The term C_w accounts for the effective liquid-vapor interface surface area due to the presence of the wick pores of diameter D_p and of the screen wires of diameter D_w.

Supplemental Relations

Supplemental relations can be used to derive relations between the liquid and vapor at the interface. Using the kinetic theory for interphase mass transfer [46] and the Clausius-Clapeyron Equation [47], the radial liquid velocity at the liquid-vapor interface is

$$\begin{aligned}
V_0 &= \sqrt{\frac{M}{2\pi R_u}} \left[\frac{\rho_v}{\rho_l} h_{fg}\right][T_v^{-3/2}](T_v - T_s) \\
&= h_1 [T_v^{-3/2}](T_v - T_s)
\end{aligned} \tag{65}$$

77

The interphase heat flux can be expressed by using the continuity equation and substituting Eq. (65) in Eq. (64)

$$q_0 = C_w \sqrt{\frac{M}{2\pi R_u}} \left[\rho_v h_{fg}^2\right] [T_v^{-3/2}](T_v - T_s) \tag{66}$$

7.2 THE VAPOR PHASE MATHEMATICAL FORMULATION

Heat pipe dynamics are strongly dependent on the vapor phase so that complete solution of the heat pipe problem requires solution of the full system of vapor phase governing equations. The intent of this research was to develop a computational algorithm for liquid phase dynamics that would be combined with a vapor phase algorithm. Development of the vapor phase algorithm encountered extreme difficulties such that a vapor code was not available for complete checkout of both the liquid and vapor codes at the time this work was done, see [44]. An approximation of the vapor phase was developed to permit demonstration of the liquid phase code operation.

The characteristics of vapor flow allow some simplification in developing the approximate model. In general the vapor response is orders of magnitude faster than the liquid response such that the vapor can possibly be treated as quasisteady in a liquid time scale reference [31]. The vapor is also assumed to be uniform in a selected control volume. A mass balance on the control volume for a single arbitrary time step gives

$$M_v^{(n+1)} = M_v^{(n)} - \delta_t \dot{m}_v \tag{67}$$

where M_v is the total vapor mass at a given discrete time. δ_t is the time step size. and $\dot{m}_v$ is the net mass flux due to evaporation and condensation. The sign of $\dot{m}_v$ is taken such that evaporation, which has a negative velocity, produces mass addition, while condensation produces mass extraction from the vapor space.

Solution of Eq. (67) can be used to fix the vapor state. The solution is dependent on the phase change process, which is a function of the heat pipe operating limits. This study will consider restriction only due to the sonic limit. The solution is then dependent on whether the pipe operation is subsonic or sonic limited.

7.2.1 Subsonic Vapor Operation

Subsonic operation is assumed to occur such that the vapor is uniform at a given time step. The mass balance control volume is then the entire vapor space. The net phase change mass transfer can be expressed as

$$\dot{m}_v = \int_0^L \rho_v V_{0v} C_w 2 \pi R_v dx \tag{68}$$

Using the continuity equation (Eq. (61)) and the kinetic energy formulation for V_0 (Eq. (64)) gives

$$\dot{m}_v = C_w R_v \sqrt{\frac{2\pi}{R_g}} \rho_v h_{fg} \left[L T_v^{-1/2} - T_v^{-3/2} \int_0^L T_s dx \right] \tag{69}$$

where T_v is the uniform vapor temperature, T_s is the liquid-vapor interface surface temperature, and R_g is the gas constant for the working fluid of interest. As a first approximation, all parameters except the temperatures in Eq. (69) are assumed to be at time level $t^{(n)}$.

Substituting Eq. (69) in Eq. (67) and dividing by the fixed volume of the vapor space V gives

$$\rho_v^{(n+1)} = \rho_v^{(n)} \left\{ 1 - \frac{\delta_l C_w R_v}{V} \sqrt{\frac{2\pi}{R_g}} \, h_{fg} \left[L T_v^{-1/2} - T_v^{-3/2} \int_0^L T_s \, dx \right] \right\} \tag{70}$$

The Clausius-Clapeyron Equation can be solved for the vapor density to give

$$\rho_v = \left[\frac{h_{fg}}{T \left(\dfrac{dP}{dT} \right)_{sat}} + \frac{1}{\rho_l} \right]^{-1} \tag{71}$$

All parameters except temperature are again assumed to be from time level $t^{(n)}$.

Equations (70) and (71) can be equated to produce a nonlinear expression for T_v in terms of time level $t^{(n)}$ properties and time level $t^{(n+1)}$ liquid-vapor interface surface temperatures. The equation can be solved using Newton's method.

80

7.2.2 Sonic Limit Operation

The sonic limit condition is a restriction on axial mass and heat transfer. This restriction implies that the entire vapor space cannot be treated as uniform. The vapor space will be approximated as two control volumes. The first control volume is the vapor space of the evaporator. The second control volume consists of the combined vapor space of the adiabat and condenser regions. The two control volumes communicate through the axial vapor transport corresponding to sonic limited operation. The control volume mass balance for the evaporator is

$$M_{ve}^{(n+1)} = M_{ve}^{(n)} - \delta_t \dot{m}_{ve} - \delta_t \dot{m}_{son} \tag{72}$$

and for the adiabatic-condenser is

$$M_{vc}^{(n+1)} = M_{vc}^{(n)} - \delta_t \dot{m}_{vc} + \delta_t \dot{m}_{son} \tag{73}$$

where $\dot{m}_{son}$ is the sonic limit axial vapor flux. The heat flux associated with the sonic limit as a function of vapor properties at the point of sonic velocity is approximated by [8]

$$Q_{son} = \frac{\rho_v \, h_{fg} \, A_v \, c}{\sqrt{2(1 + \gamma)}} \tag{74}$$

The sonic limit mass flux can be derived from the sonic limit heat transfer given by Eq. (74). Solving for mass transfer of sodium vapor produces

$$\dot{m}_{son} = \pi R_v^2 \sqrt{\frac{5R_g}{16}} \, \rho_v \sqrt{T_v} \tag{75}$$

81

The phase change mass flux for each control volume is found from Eq. (68) with limits of integration corresponding to the respective control volume. The evaporator control volume has phase change mass flux of

$$\dot{m}_{ve} = \int_0^{L_e} \rho_v V_{0v} C_w 2\,\pi\,R_v dx \tag{76}$$

or

$$\dot{m}_{ve} = C_w R_v \sqrt{\frac{2\pi}{R_g}}\,\rho_v h_{fg} \left[L_e T_v^{-1/2} - T_v^{-3/2} \int_0^{L_e} T_s dx \right] \tag{77}$$

Phase change mass flux for the adiabatic-condenser control volume is

$$\dot{m}_{vc} = \int_{L_e}^{L} \rho_v V_{0v} C_w 2\,\pi\,R_v dx \tag{78}$$

or

$$\dot{m}_{vc} = C_w R_v \sqrt{\frac{2\pi}{R_g}}\,\rho_v h_{fg} \left[(L - L_e) T_v^{-1/2} - T_v^{-3/2} \int_{L_e}^{L} T_s dx \right] \tag{79}$$

Equations (72) and (73) can be solved using Eqs. (75), (77) and (79) for the vapor density during sonic limit conditions for each of the control volumes. Using the Clausius-Clapeyron Equation as in the subsonic case produces a nonlinear expression for vapor temperature in each control volume that can be solved with Newton's method.

82

7.3 THE COMPUTATIONAL IMPLEMENTATION

The governing equations, boundary conditions, property relations, and supplemental equations were coded for solution in a Fortran computer program. The calculations are performed at discrete grid points in the liquid and pipe wall. For clarity, the program first will be presented in a top level sense to establish the overall sequence of calculation. The detailed algorithm will then be discussed. Equations presented in other sections of the thesis are repeated when discussed below for convenience.

Overall organization of the program is shown in the flowchart in Figure 20. The algorithm begins by setting various parameters and initializing conditions. The time stepping section is then entered. Operating limits and property dependent parameters are updated. The input heat flux is updated as is the vapor regime. The iteration section is then entered. The first partial time step (t^*) is solved for liquid and pipe temperatures, vapor temperature, and liquid velocities. The same steps are then repeated for the second partial time step ($t^{(n+1)}$). Iterations are repeated on the first and second time split equations until temperatures of the liquid surface and container wall have converged to a user specified tolerance. After time step convergence the thermophysical properties are updated. Heat transfer limits are determined. Input, output, evaporation, and condensation heat transfer rates are calculated. The capillary limit heat transfer is calculated and compared to evaporation heat transfer. A stop flag is set if the limit is exceeded. A steady state test is performed by comparing input and output heat fluxes. Flags are set if steady state is reached. The liquid pressure gradient and liquid pressures are evalu-
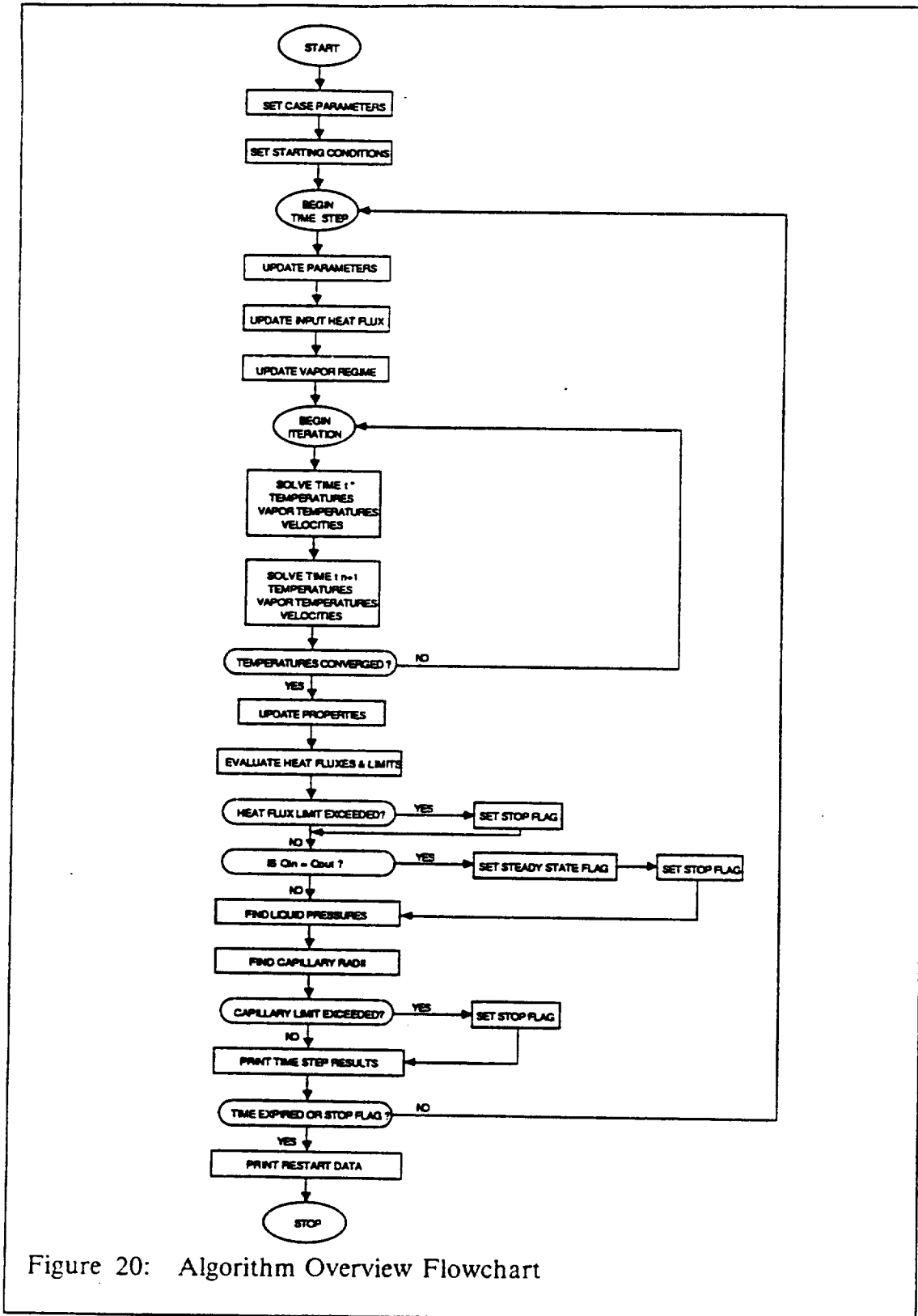
Figure 20: Algorithm Overview Flowchart

ated. The capillary radii are determined from vapor pressure, liquid pressure, and phase change velocities. Capillary radii are checked for the capillary pumping limit. A stop flag is set if the capillary limit is exceeded. Time step data are printed, and the program advances to the next time step unless a stop flag was issued or time has expired. If calculations are to be terminated, restart data are printed to a restart file which can be used to continue the calculations in a later run.

7.3.1 *Details of the Numerical Procedure*

The detailed program can be considered in three broad sections: the startup section, the iteration section, and the completion section. The startup section shown in Figure 21 begins the calculation cycle. Calculations can be performed beginning from a time zero condition or in restart mode to continue calculations of a previous case. The algorithm begins by setting common and dimension areas, and reading input data. Input data consist of the restart option flag, time step size, grid step sizes, vapor space radius, wick pore radius, screen wire radius, environment heat sink radiation temperature, and initial heat pipe temperature. The restart option flag controls the program initialization steps so that for a restart case, the program will initialize with the appropriate data from the previous case. Geometry parameters are calculated. Time parameters controlling the duration of the calculations are set. Data output print control parameters are set. Heat pipe surface radiation characteristics are set as are input heat flux control parameters used in Eqs. (80) and

(81). Thermophysical properties of the pipe wall material and sodium working fluid properties are initialized. Combinations of various constants used repeatedly throughout the code are calculated to reduce total arithmetic. Peaceman-Rachford ADI parameters, operating limits and temperature and velocity fields are initialized. Startup data are printed, and control passes to the beginning of the time steps in the iteration section.

The iteration section shown in Figure 22 begins the time step and performs iterations between temperatures and velocities until acceptable convergence is achieved. Property dependent operating limits and ADI parameters are updated. Input heat flux is updated for the new time step. The input heat flux profile and time dependence are user defined functions

$$t \leq \tau$$

given by Eqs. (80) and (81)

$$q_{in} = \frac{1}{2} q_{max} \left\{ 1 - \sin \left[\pi \left(\frac{t}{\tau} + \frac{1}{2} \right) \right] \right\} \tag{80}$$

and for

$$t > \tau$$

$$rqno(81) q_{in} = q_{max}$$

An option is included to smooth the abrupt step change of heat input at the evaporator-adiabatic boundary. The vapor operating regime is checked using Eq. (75). Operation is subsonic if axial heat transfer is below the sonic limit and is sonic limited otherwise.
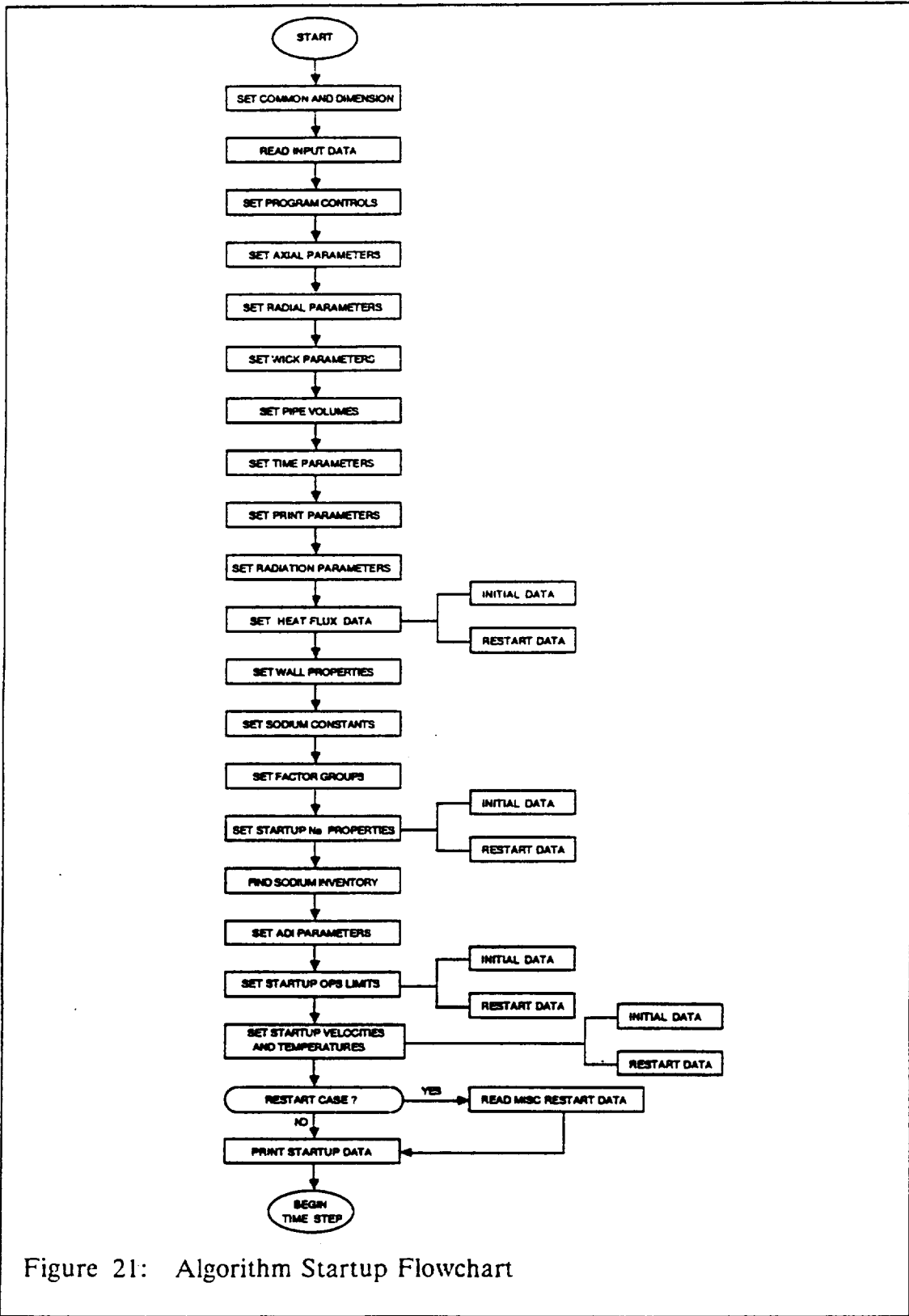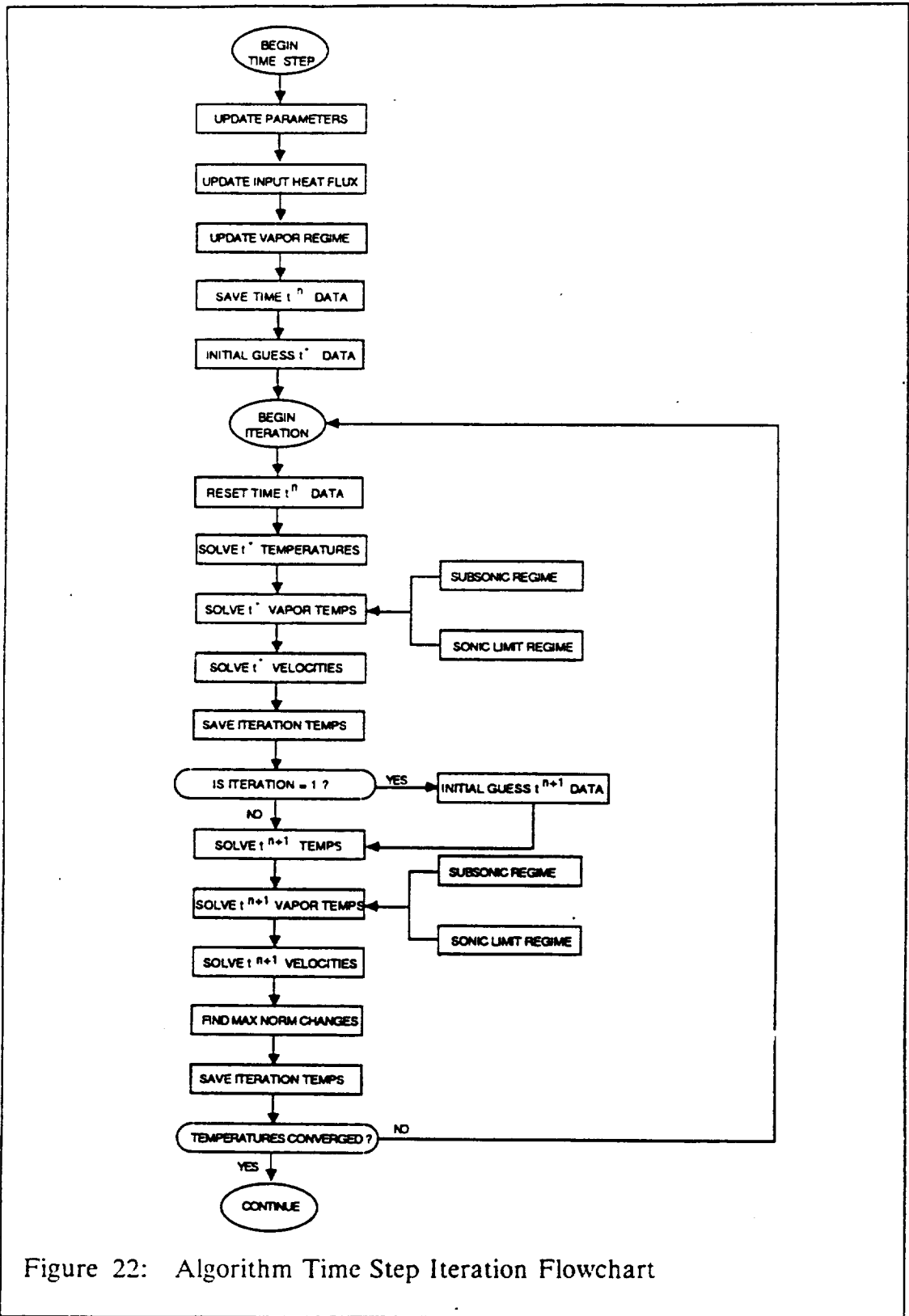
86

Figure 21: Algorithm Startup Flowchart

Figure 22: Algorithm Time Step Iteration Flowchart

Iterations are set up by saving data from the just completed time step and using these data as the initial guess for the next time step. Iterations are performed by first solving for time t^* liquid and container temperatures. The finite difference Peaceman-Rachford Alternating Direction Implicit method is used to solve the energy equation in two partial time steps. The method essentially involves solution by integrating the energy equation for a partial time step (time t^*) in the radial direction, and then integrating for the remaining time step (time $t^{(n+1)}$) in the axial direction.

The first time split liquid temperatures are then used to find time t^* vapor temperatures. Depending on whether the vapor is subsonic or sonic limited, control passes to the appropriate subroutine to use Newton's method to solve the vapor temperature equation. Subsonic vapor temperature is determined from Eqs. (70) and (71). Sonic limited vapor temperatures are determined from Eqs. (71), (72), and (73). Based on vapor temperatures and liquid-vapor interface surface temperatures the liquid phase change velocity is calculated from Eq. (65). The bulk axial velocity distribution is calculated from the continuity equation and the liquid phase change velocity using the following equation.

$$\overline{U}(i) = \frac{1}{2} \frac{A_{lv}}{A_a} \left[V_0(1) + 2 \sum_{n=2}^{i-1} V_0(n) + V_0(i) \right] \tag{82}$$

Bulk axial velocity is transformed to a velocity profile using the following equation

$$u^* = a + b\,r^* + c\,r^{*2} + d\,r^{*3} \tag{83}$$

Finally, the radial velocity distribution is found from an equation given below

$$v(x,r) = \frac{C_w V_0 R_v}{r}\left\{ 1 - \frac{2\delta}{R_l + R_v} \right.$$
$$\left. \left[b\frac{R_v}{\delta}\frac{r^{*2}}{2} + \left(b + c\frac{R_v}{\delta} \right)\frac{r^{*3}}{3} + \left(c + d\frac{R_v}{\delta} \right)\frac{r^{*4}}{4} + d\frac{r^{*5}}{5} \right] \right\} \tag{84}$$

Then, calculations for the first time split are completed.

The second time split is set up by setting the temperatures and velocities for the first iteration of the ($t^{(n+1)}$) time split equal to the time t^* values. The liquid and container temperatures, vapor temperatures, and velocities for the second partial time step ($t^{(n+1)}$) are found as in the first time split with liquid and container temperatures found using the ADI equation

$$A_4 T_{i-1,j}^{(n+1)} + A_5 T_{i,j}^{(n+1)} + A_6 T_{i+1,j}^{(n+1)} = B_4 T_{i,j-1}^* + B_5 T_{i,j}^* + B_6 T_{i,j+1}^* \tag{85}$$

The energy equation and the flow dynamics equations are tightly coupled at the liquid-vapor interface such that the solutions of each are interdependent. In addition, the equations contain nonlinear terms that required quasilinearization treatment, which requires iterations. Iterations are performed between temperatures and velocities until an acceptable convergence is achieved.

The completion section of the program shown in Figure 23 includes all remaining functions to complete the time step calculations and send control to the next time step or terminate execution. Thermophysical properties are up-

dated based on the temperature conditions. A mass balance is performed to track working fluid inventory. The sonic limit heat transfer is determined from Eq. (74). Capillary limit heat transfer is determined from

$$\left.\frac{\Delta P}{\Delta x}\right|_{cap} = -F_l Q_{cap} \qquad (86)$$

Input, output, evaporation, and condensation heat transfer rates are evaluated. A stop flag is issued if the capillary limit is exceeded. Input heat transfer is compared with output heat transfer, and a steady state flag is issued if they are approximately equal.

Liquid pressures are found from the following equation which is found from the axial momentum integral equation

$$\begin{aligned}
P_i^{(n+1)} &= P_{i+1}^{(n+1)} + P_{i+1}^{(n)} - P_i^{(n)} \\
&\quad - \left[\frac{\mu}{h_x}\overline{U}_{i-1} + \left(\gamma h_x - \frac{2\rho h_x}{k} - \frac{2\mu}{h_x}\right)\overline{U}_i + \frac{\mu}{h_x}\overline{U}_{i+1}\right]^{(n+1)} \\
&\quad - \left[\frac{\mu}{h_x}\overline{U}_{i-1} + \left(\gamma h_x + \frac{2\rho h_x}{k} - \frac{2\mu}{h_x}\right)\overline{U}_i + \frac{\mu}{h_x}\overline{U}_{i+1}\right]^{(n)}
\end{aligned} \qquad (87)$$

The integration is performed by assuming liquid pressure and vapor pressure are equal at the end of the condenser $(x = L)$. The liquid-vapor interface radial momentum condition given by Eq. (63) can be solved for the capillary radii of curvature to give

$$R_c = \frac{2\sigma}{P_v - P_l + (\rho_l V_0)^2\left[\frac{1}{\rho_v} - \frac{1}{\rho_l}\right] + 2\mu_l\frac{\partial V_0}{\partial r}} \qquad (88)$$
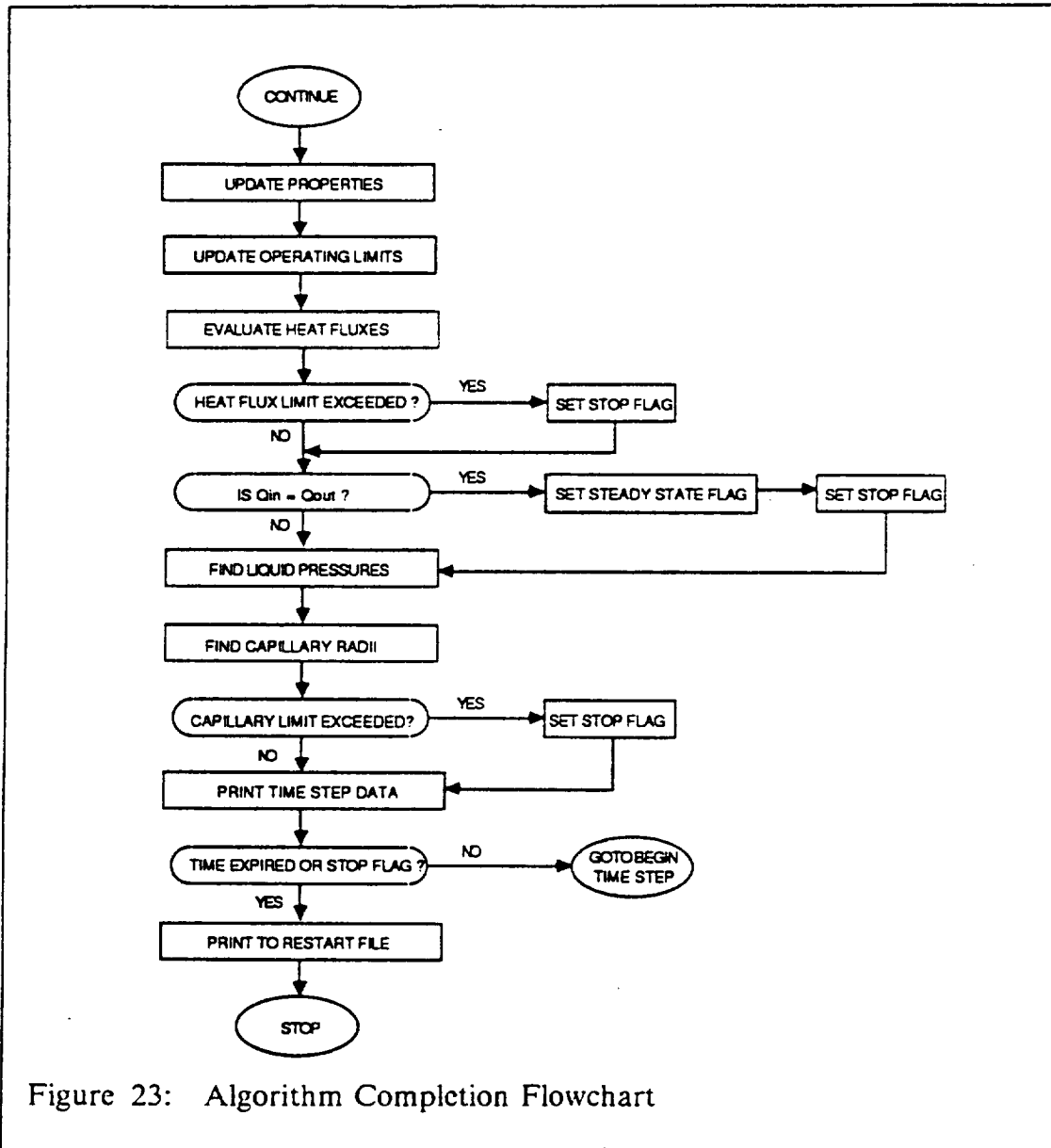
91

Figure 23: Algorithm Completion Flowchart

The total liquid pressure drop is compared to the maximum possible capillary

pumping capability of the wick.is given by

$$\Delta P_{cap} = \frac{2\sigma}{R_p} \qquad (89)$$

A stop flag is activated if the limit is exceeded. Data from the time step are printed, and the next time step is initiated unless a stop flag has been activated or time for the case has expired. Data from the final time step are dumped to a restart file, and execution is terminated.

7.4 SOME RESULTS

Capabilities of the computational algorithm were tested by running two heat pipe startup cases. The heat pipe dimensions were chosen to be consistent with the experimental device described by Merrigan et al. up to the limit of the uniform grid used in this analysis [27,28]. The experimental heat pipe in that study used lithium as the working fluid and an annular wick configuration. The annular region for liquid flow was formed between the pipe interior wall and a porous concentric tube constructed of 7.25 layers of pressed screen. The high temperatures involved required the container to be constructed from the refractory alloy molybdenum. The heat pipe geometry parameters used in this analytical study compared to the actual parameters are (see Figs. 18 and 19):

Parameter	Actual	Approximate
Heat Pipe Internal Length (L)	4.0	4.0 m
Evaporator Length (L_e)	0.4 m	0.4 m
Condenser Length (L_c)	3.0 m	3.0 m
External Diameter (D_w)	1.90 cm	1.886 cm
Internal Diameter (D_l)	1.60 cm	1.598 cm
Vapor Space Diameter (D_v)	1.49 cm	1.490 cm

Effective Wick Pore Diameter (D_p) 53 μm   53 μm

where the effective wick pore diameter was experimentally determined from surface tension measurements.

An axial grid step size of $h_x = 0.2$ m and a radial grid step size of $h_r = 1.1 \times 10^{-4}$ m were used. The computational grid consisted of 21 axial grid steps and 20 radial grid steps. The grid mapping to the heat pipe configuration is:

Radial Liquid Space	$1 \leq j < 6$
Radial Pipe Wall	$6 \leq j \leq 20$
Axial Evaporator Region	$1 \leq i \leq 3$
Axial Adiabatic Region	$3 < i < 6$
Axial Condenser Region	$6 \leq i \leq 21$

Numerical experimentation showed that the code is highly sensitive to time step size. Too large a time step produced an inconsistent temperature at the liquid-vapor interface. The temperature was inconsistent in that the temperature gradient at the surface changed sign relative to the gradient of the interior liquid. For example, in the evaporator energy is conducted from the pipe wall to the liquid-vapor interface. The liquid-vapor surface temperature should be the lowest temperature in the radial conduction path in order for the energy to reach the surface. Too large a time step will produce a physically

94

questionable surface temperature that is greater than the temperature of the interior liquid. Too large a time step was also found to cause oscillations in the pressure calculations.

The time step size was selected by running a series of calculations for three hundred time steps each with gradually decreasing step sizes. A time step size of $\delta_t = 2 \times 10^{-3}$ second was found to eliminate inconsistent liquid-vapor interface temperatures, but did not completely remove pressure oscillations. A time step size of $\delta_t = 1 \times 10^{-3}$ second removed the pressure oscillations for the three hundred time steps calculation. This time step was used in the calculations.

7.4.1 Slow Startup Test

A startup test was devised to supply input energy to the evaporator such that the heat pipe would warm up without reaching the sonic limit. This test was to check overall program implementation. Input heat flux was supplied according to the function

$$t \leq \tau$$

$$q_{in} = \frac{1}{2} q_{max} \left\{ 1 - \sin \left[\pi \left(\frac{t}{\tau} + \frac{1}{2} \right) \right] \right\} \qquad (90)$$

$$t > \tau$$

$$q_{in} = q_{max} \qquad (91)$$

where q_{max} is the maximum input heat flux and τ is the time stretching parameter that controls how quickly q_{in} reaches q_{max}. In this test, $q_{max} = 1 \times 10^6$ W/m^2 and $\tau = 300$ seconds corresponding to a five minute period for the input heat flux to reach the maximum.

Calculations were performed for 114,193 time steps, or a period slightly greater than 114 seconds. The run was terminated at this time since the liquid pressure drop exceeded the capillary pumping limit. The liquid pressure drop and the capillary pumping limit as functions of time are shown in Figure 24. Analysis of the results shows that the capillary pumping limit was exceeded due to a large jump in pressure drop at a single time step. Figure 24 also shows that the pressure calculations had been experiencing oscillations with usually small amplitudes of approximately 2.5 Pa. The oscillations began after the 300 time steps used to verify the adequacy of the time step size of 1×10^{-3} second. The liquid pressure drop curve is drawn through the centers of the oscillation ranges in Figure 24. The oscillations become very large at $t = 90$ seconds, but begin to decay until the large jump occurs at approximately 114 seconds.

Figure 24: Slow Startup Pressure Drop Results
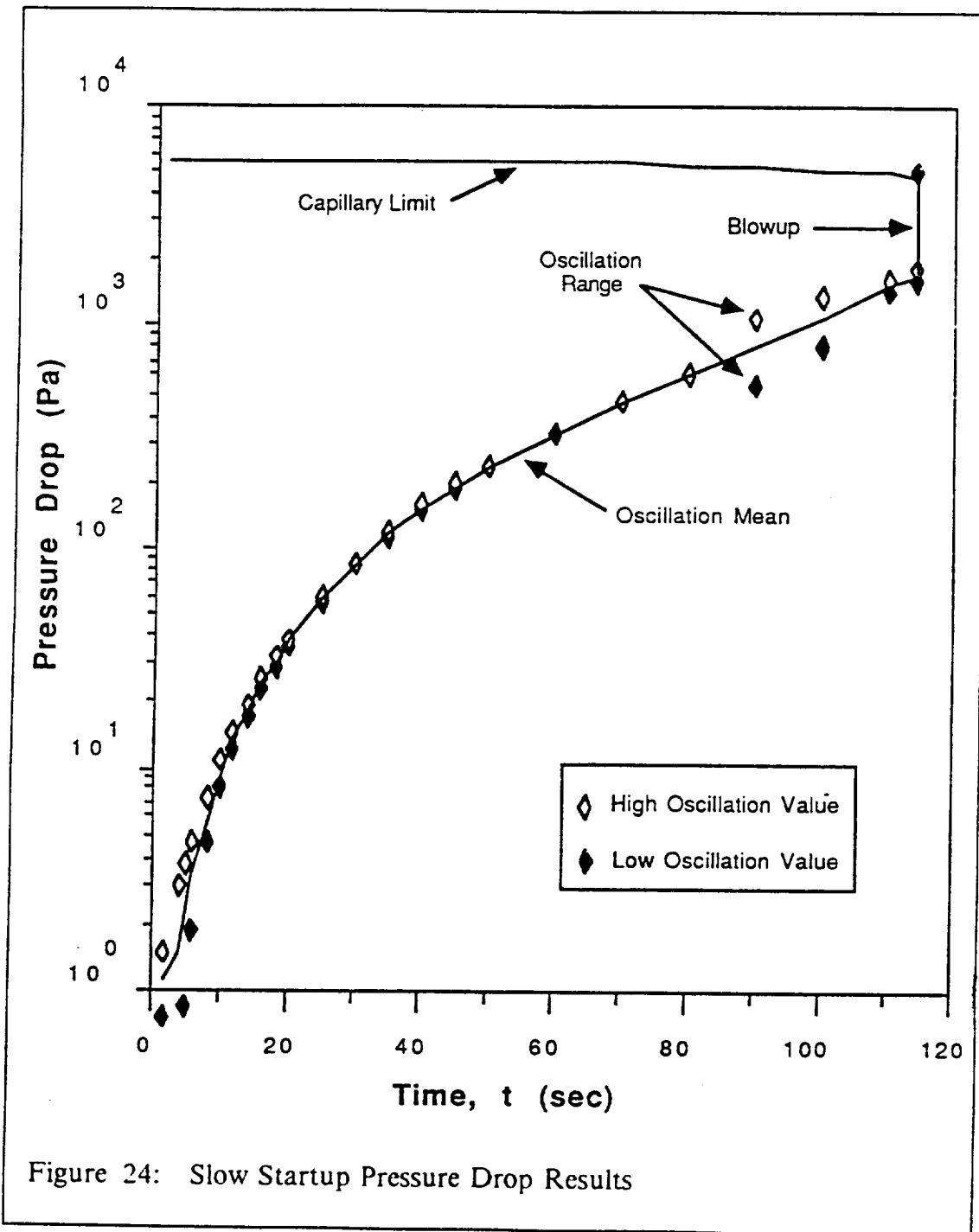
The pressure oscillations are presented in detail in Figure 25. The liquid

pressure drop is plotted for eleven consecutive time steps for

$19,990 \leq k \leq 20,000$, corresponding to the time around time $t = 20$ seconds in Figure 24. The oscillations are of essentially constant amplitude and well behaved until time $t > 80$ seconds as shown in Figure 24.

Figure 25:   Slow Startup Liquid Pressure Drop Oscillations
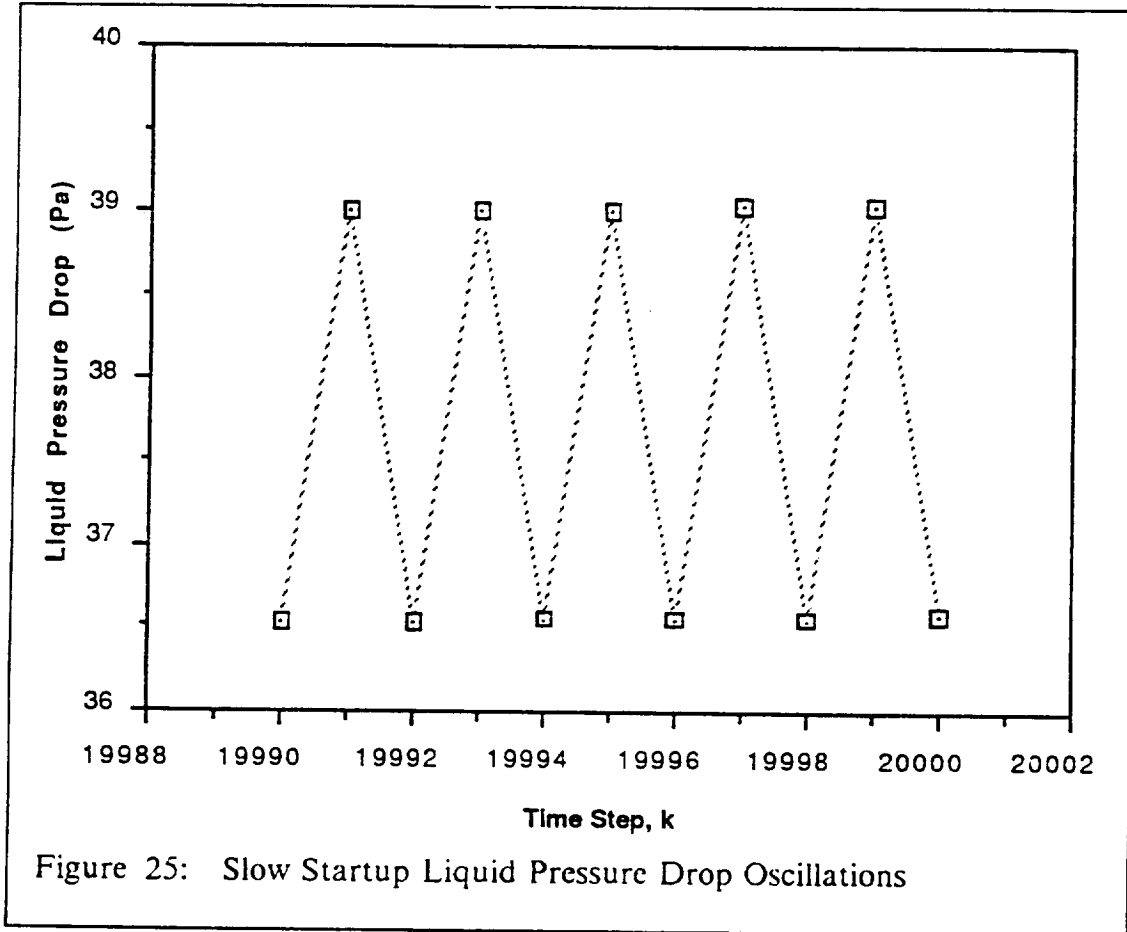
Power transfer as a function of time is shown in Figure 26. While the input power briefly exceeds the sonic limit line, the phase change heat transfer remains below the sonic limit. At approximately 103 seconds into the transient, the sonic limit exceeds the capillary limit so that the capillary limit becomes the controlling heat transport limit. At approximately 105 seconds, the unlikely result is produced that the phase change heat transfer exceeds the input heat

transfer. With the exception of this anomaly, the heat transfer curves are well behaved, smooth functions of time. In addition, the phase change heat transfer is well below the capillary limit heat transfer at the point when liquid pressure drop jumps to exceed the capillary pumping limit. The cause of the liquid pressure drop jump is not apparent from the heat transfer curves.

The vapor temperature as a function of time is shown in Figure 27. The vapor temperature is also a smooth, although rapidly increasing, function of time. The cause of the jump in liquid pressure drop is also not apparent from vapor temperature.

The pressure drop calculation can be seen in Figure 24 to produce oscillatory behavior with large sporadic oscillations for time greater than 80 seconds. The pressure calculations are a sensitive function of time step size. Numerical experimentation also showed that the pressure calculations are sensitive to property updates and changes in the liquid-vapor interface boundary conditions corresponding to the change between subsonic and sonic limited operation. Sensitivity to property updates was identified by varying the frequency at which updated properties are calculated.

There are many potential causes for the pressure oscillations. The pressure oscillations may be physical, but this possibility is remote considering the numerical sensitivities of the method. The time step size of 1×10^{-3} second may have been too large. If this is the case, a smaller time step may not be acceptable considering the cost of computations for a transient process that occurs over a period of tens of minutes. The oscillations may have resulted from the derivation of the axial velocity profile in which the shape is determined by
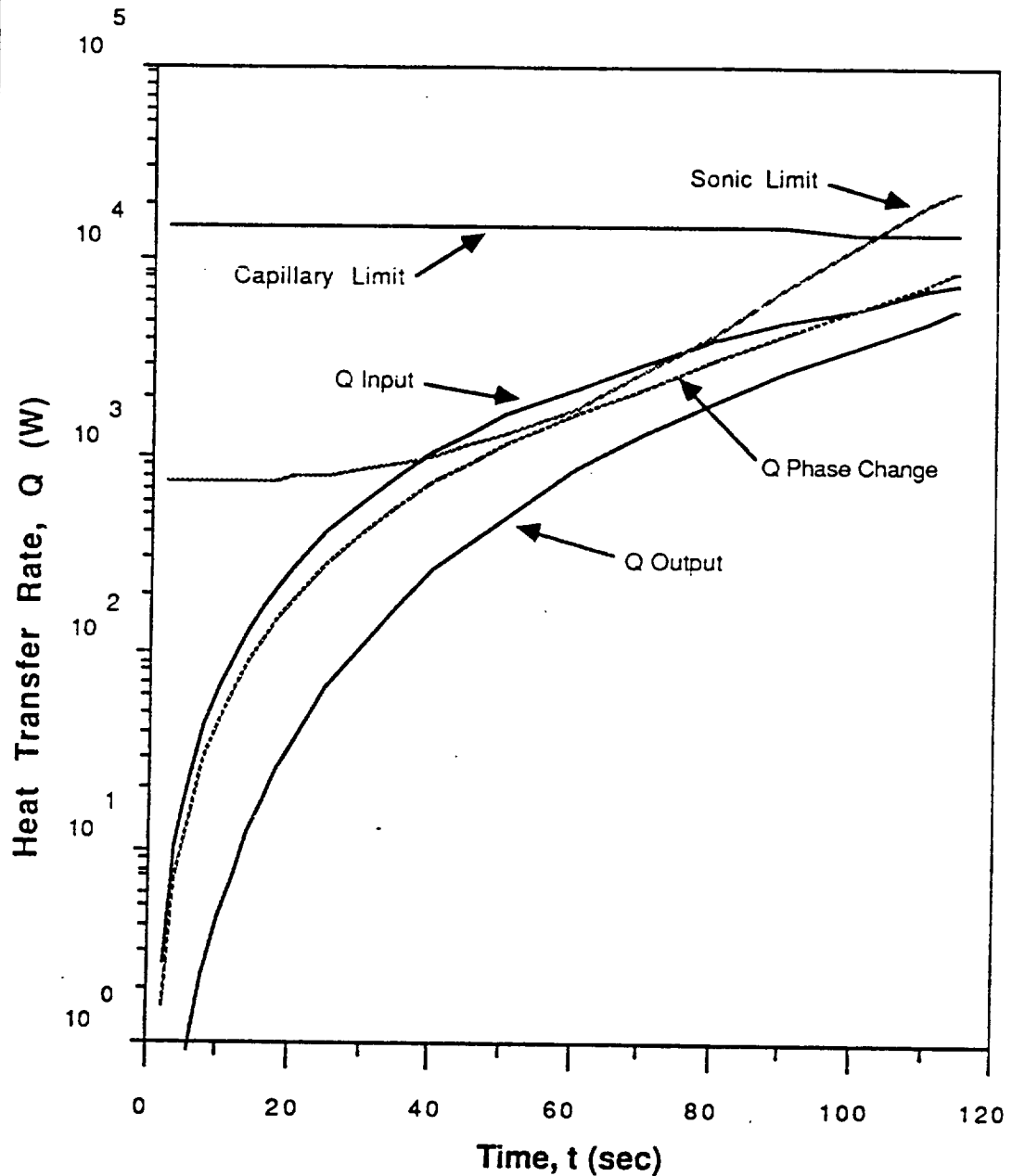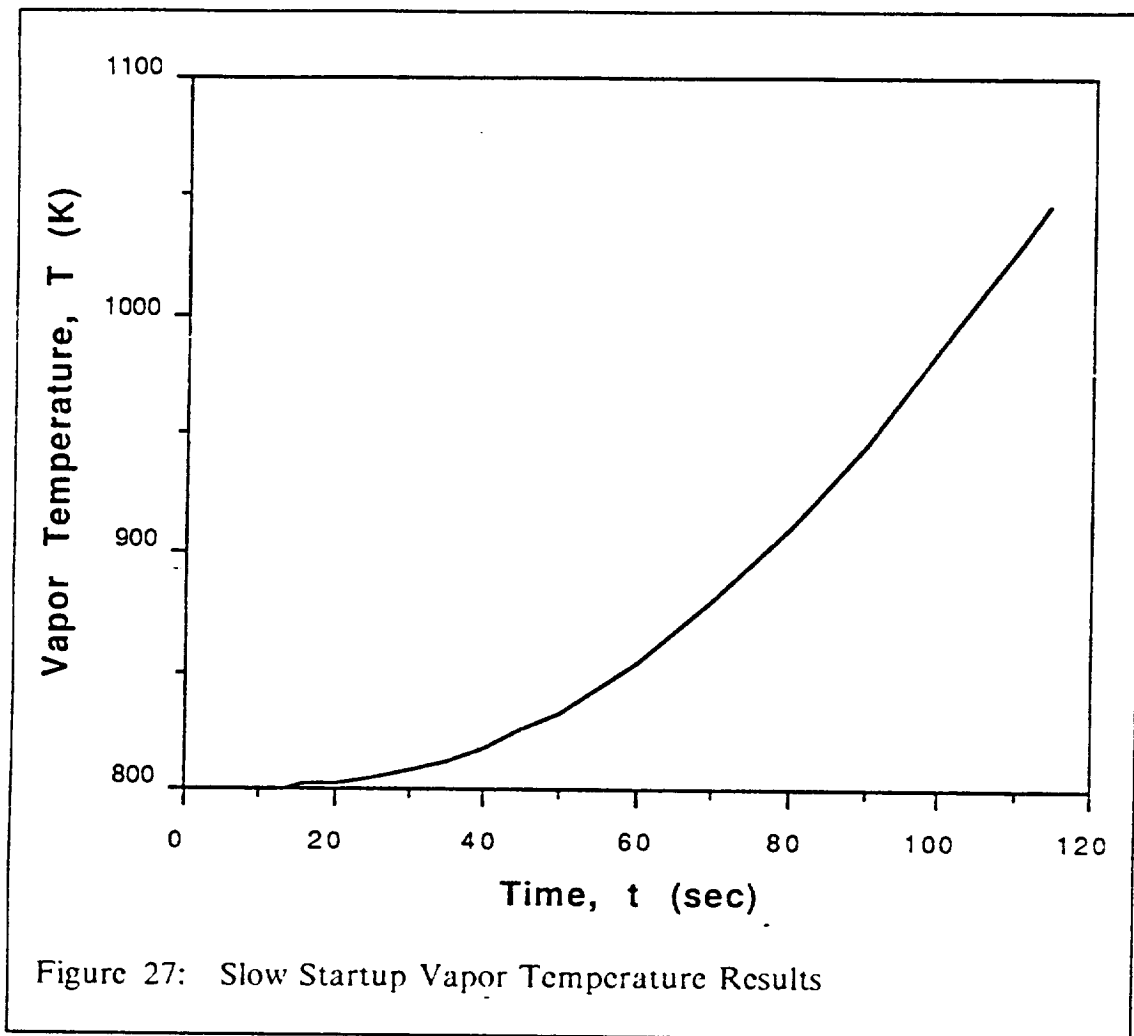
Figure 26:   Slow Startup Heat Transfer Results

neglecting the temporal terms in the momentum equation. The pressure cal-

culations are also based on the convenient assumption that the minimum liq-

Figure 27:   Slow Startup Vapor Temperature Results

uid pressure occurs at the end of the condenser, although this assumption is not generally valid for the wide range of operating conditions encountered during a startup transient.

7.4.2 Sonic Limit Startup Test

A startup test was performed to test algorithm calculation of sonic limited operation. Using again $\tau = 300$ seconds, the maximum input heat flux was increased to $q_{max} = 1.5 \times 10^6$ W/m^2 to assure the phase change heat transfer would reach the sonic limit. Heat transfer results are shown in Figure 28.

Input power exceeds the sonic limit at 20 seconds, and remains above the sonic limit through the duration of the test of 130 seconds. The evaporation and condensation heat fluxes are essentially equal as the sonic limit is reached at approximately 40 seconds. Evaporation and condensation follow the sonic limit curve until 80 seconds. After 80 seconds, condensation heat flux increases above the sonic limit, while evaporation heat flux continues to follow the sonic limit curve. This unlikely result is a result of the inadequacies of the simple vapor model used to perform calculations. The vapor model unintentionally forces a high condensation rate, which forces the condenser temperature to increase rapidly due to the high thermal resistance of the radiation boundary condition on the condenser. This temperature effect is shown in Figure 29. The evaporator vapor temperature smoothly and gradually increases with time, while the condenser vapor temperature rapidly increases. The condenser temperature eventually increases sufficiently so that radiation heat transfer from the condenser becomes very efficient. At approximately 93 seconds, the output heat transfer exceeds the evaporation heat transfer, which is another unlikely result. Calculations are terminated at 130 seconds due to the condensation heat transfer exceeding the capillary heat transfer limit. While the capillary limit is not strictly a limit on condensation, calculations
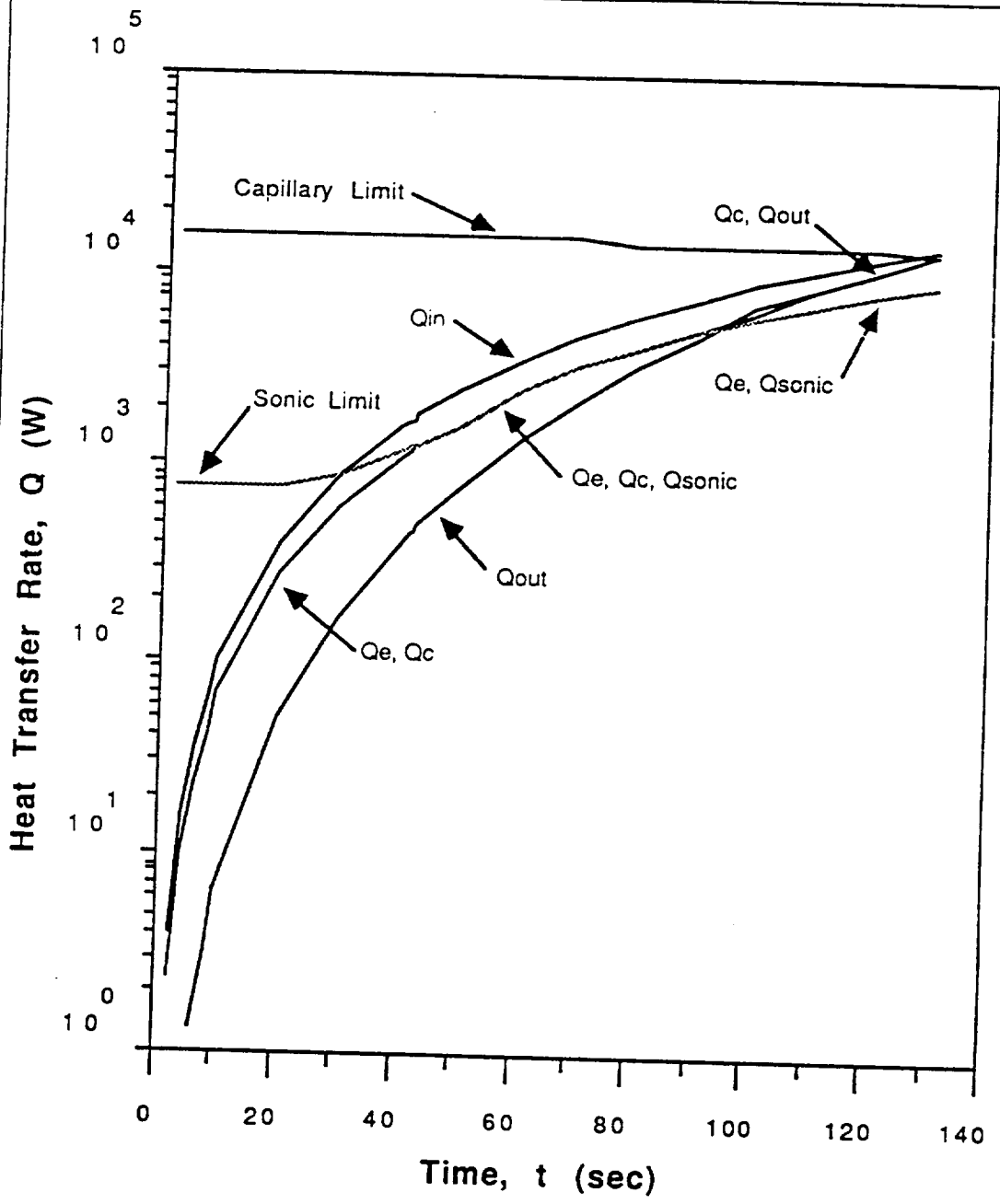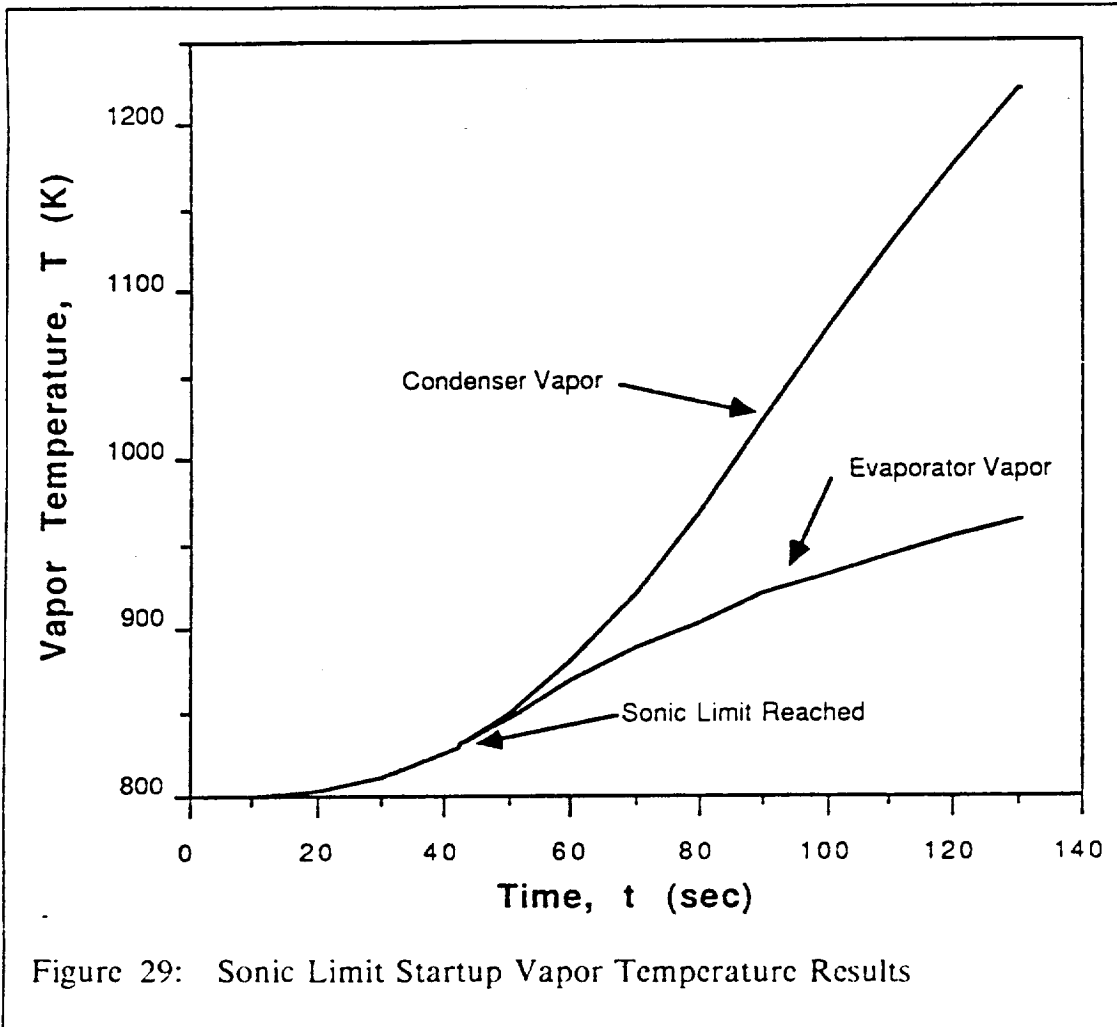
Figure 28: Sonic Limit Startup Heat Transfer Results

had already passed beyond physical significance and the computational implementation had been demonstrated.

Figure 29: Sonic Limit Startup Vapor Temperature Results

7.5 CONCLUSIONS AND RECOMMENDATIONS

The heat pipe is a very complex device such that performing analysis of heat pipe transients is a difficult venture. The difficulty is due to the coupled liquid and vapor dynamics, the phase change process, the coupled heat transfer problem with nonlinear boundary conditions, the physical geometry, and the transient time requirement. This study has presented the full system of governing equations, including boundary conditions, required to solve the liquid

phase heat pipe problem. A simplified solution was formulated by using certain assumptions and integrating the liquid dynamics equations.

The resulting formulation identified a key requirement for future research in solving the heat pipe problem. This study used a kinetic theory approach to model the phase change process as expressed by Eq. (65). The model consists of a large coefficient multiplying a very small temperature difference. The model requires a very small time step for stability even with the simplifications used in this analysis. The large coefficient also transforms temperature differences that are otherwise beyond machine accuracy into computationally significant terms. Future research should investigate an alternative model for the phase change process.

Difficulty with geometry was encountered due to the widely disparate length scales in the different coordinate directions. The radial dimension across the liquid is much smaller than the radial dimension across the pipe wall, which in turn is much smaller than dimensions in the axial direction. One approach to address this problem is to assume radial gradients are negligible. The radial pressure gradient was neglected in this study. This study also found small radial temperature gradients indicating that the radial thermal resistance is small. The drawback of this approach is the loss of fidelity with the true physics of the problem. A preferable approach may be to use a variable mesh grid with a to-be-determined simplified treatment of radial gradients. The variable mesh grid allows fine resolution in important regions with coarse resolution in the other regions. The simplified treatment of radial gradients would take advantage of the small radial gradients.

105

The long duration of transients presents a competing concern with model complexity. An overly complex model with high fidelity may be too computationally expensive for practical calculations of transients.

This study has also shown that the transient heat pipe problem is not amenable to a straightforward simplification such as is used for the vapor phase. The solution of the heat pipe transient problem requires a full solution of the liquid and vapor phases. This elusive solution is left to future efforts.

REFERENCES

1. Gaugler, R. S., *Heat Transfer Device*, US Patent No. 2,350,348, 1942.

2. Grover, G. M., Cotter, T. P., Erickson, G. F., "Structures of Very High Thermal Conductance", *J. Appl. Phys.*, 35, No 6, pp 1990-1991, 1964.

3. Cotter, T. P., "Theory of Heat Pipes", *LA - 3246 - MS*, 1965.

4. Ranken, W. A., "Heat Pipe Development for the SPAR Space Power System", in *Advances in Heat Pipe Technology*, Reay, D. A., Ed., Pergamon Press, 1981.

5. Camarda, C. J., "Aerothermal Tests of a Heat-Pipe-Cooled Leading Edge at Mach 7, *NASA-1320*, 1978.

6. DeMeis, R., "Heat Pipe Cooled Rockets", *Aerospace America*, 25, No. 3, 1987.

7. Dunn, P., Reay, D. A., *Heat Pipes*, 3rd ed., Pergamon Press, London, 1982.

8. Chi, S. W., *Heat Pipe Theory and Practice: A Sourcebook*, Hemisphere, Washington, 1976.

9. Busse, C. A., "Heat Pipe Research in Europe", *Proc., 2nd Int. Conf. on Thermionic Electrical Power Generation*, Stresa, Italy, May 1968.

10. Levy, E. K., "Theoretical Investigation of Heat Pipes", *Proc., Aviation and Space Conf.*, Beverly Hills, California, pp 671-676, 1968.

11. Levy, E. K., "Effect of Friction on the Velocity Limit in Sodium Heat Pipes", *AIAA Paper No. 71-407*, 1971.

12. Edwards, D. K. and Marcus, B. D., "Heat and Mass Transfer in the Vicinity of the Vapor-Gas Front in a Gas-Loaded Heat Pipe", *J. Heat Transfer*, 94, No. 2, pp 155-162, 1972.

13. Brovalsky, Y. M., Bystrov, P. I. and Melkinov, M. V., "The Method of Calculation and Investigation of High-Temperature Heat Pipe Characteristics Taking into Account the Vapor Flow Compressiblity, Friction and Velocity Profile", *Proc., 2nd Int. Heat Pipe Conf.,* pp 113-122, 1976.

14. Bankston, C. A. and Smith, H. J., "Incompressible Laminar Vapor Flow in Cyliderical Heat Pipes", *ASME Paper No. 71-WA/HT-15,* 1972.

15. Bankston, C. A. and Smith, H. J., "Vapor Flow in Cylindrical Heat Pipes", *J. Heat Transfer,* 95, no. 8, pp 371-376, 1973.

16. McDonald, J. W., Denny, V. E. and Mills, A. F., "Evaporation and Condensation in an Enclosure in the Presence of a Noncondensible Gas", in *Heat Transfer in Low Reynolds Number Flow, ASME,* New York.

17. Rohani, A. R. and Tien, C. L., "Steady Two-Dimensional Heat and Mass Transfer in the Vapor-Gas Region of a GAs-Loaded Heat Pipe", *J. Heat Transfer,* 95, No. 5, pp 377-382, 1973.

18. Tien, C. L. and Rohani, A. R., "Analysis of the Effects of Vapor Pressure Drop on Heat Pipe performance", *Int. J. Heat Mass Transfer,* 17, pp 61-67, 1974.

19. Peterson, P. F. and Tien, C. L., "Gas-Concentration Measurements and Analysis for Gas-Loaded Thermosyphons", *Proc., Int. Sympo. on Natural Circulation, ASME HTD,* Boston, 1987.

20. Galaktionov, V. V., Parfenteva, A. A., Partnov, D. V. and Sasin, V. Y., "Vapor-Gas Front in the Condenser of a Two Dimensional Gas-Controlled Heat Pipe", *J. Eng. Phys.,* 42, pp 273-277, 1982.

21. Galaktionov, V. V. and Trukhanova, "Study of the Process of Heat and Mass Transfer in the Region of the Vapor-Gas Front in a Gas-Regulable Heat Pipe", *J. Eng. Phys.,* 48, pp 296-300, 1985.

22. Ooigen, H. V. and Hoogendoorm, C. J., "Vapor Flow Calculations in a Flat-Plate Heat Pipe", *AIAA J.,* 17, No. 11, pp 1251-1259, 1979.

23. Narayana, K. B., "Vapor Flow Characteristics of Slender Cylindrical Heat Pipes- A Numerical Approach", *Numerical Heat Transfer,* 10, pp 79-93, 1986.

24. Faghri, A., "Vapor Flow Analysis in a Double-Walled Concentric Heat Pipe", *Numerical Heat Transfer,* 10, pp 583-596, 1986.

25. Merrigan, M. A., "Heat Pipe Technology Issues", *Proc., 1st Symposium on Space Nuclear Power Systems*, Orbit Book Co., pp 419-426, Florida, 1985.

26. Merrigan, M. A., "Heat Pipe Design for Space Power Heat Rejection Applications" *Proc., 21st Intersociety Energy Conversion Conf.*, pp 1993-1998, 1986.

27. Merrigan, M. A., Keddy, E. S. and Sena, J. T., "Transient Performance Investigation of a Space Power System Heat Pipe", *Proc., AIAA/ASME 4th Joint Thermophysics and Heat Transfer Conf.*, Boston, Mass., 1986.

28. Merrigan, M. A., Keddy, E. S. and Sena, J. T., "Transient Heat Pipe Investigations for Space Power System", *LA-UR-85-3341*, 1985.

29. Costello, F. A., Montague, A. F. and Merrigan, M. A., "Detailed Transient Model of a Liquid-Metal Heat Pipe", *Proc., AIAA/ASME 4th Joint Thermophysics and Heat Transfer Conf.*, Boston, Mass., 1986.

30. Amsden, A. A. and Harlow, F. H., "KACHINA: An Eulerian Computer Program for Multifield Fluid Flows", *LA-5680*, 1974.

31. Bystrov, P. I. and Goncharov, V. F., "Starting Dynamics of High Temperature Gas-Filled Heat Pipes", *High Temperature*, 21, pp 927-936, 1983.

32. Chang, W. S., "Heat Pipe Startup from the Supercritical State", *Ph. D. Dissertation*, Georgia Institute of Technology, 1981.

33. Colwell, G. T. and Chang, W. S., "Measurement of the Transient Behavior of a Capillary Structure Under Heavy Thermal Loading", *Int. J. Heat Mass Transfer*, 27, No. 4, pp 541-551, 1984.

34. Chang, W. S. and Colwell, G. T., "Mathematical Modeling of the Transient Operating Characteristics of Low-Temperature Heat Pipe", *Numerical Heat Transfer*, 8, pp 169-189, 1985.

35. Ambrose, J. H., Chow, L. C. and Beam, J. E., "Transient Heat Pipe Response and Rewetting Behavior", *J. Thermophysics*, 1, pp 222-227, 1987.

36. Hauf, W. and Grigull, U., "Optical Methods in Heat Transfer", in *Advances in Heat Transfer*, 6, pp 134-366, 1970.

37. Mayinger F. and Panknin, W., "Holography in Heat and Mass Transfer", *Proc., 5th International Heat Transfer Conf.*, VI, pp 28-43, Japan, 1974.

38. Panknin, W., "Eine Holographische Zweiwellenlangen Interferometrie zur Messung uberlagerter Temperatur- und Konzentrationsgrenzschichten", *PHD Thesis*, Technischen Universitat Hannover, Germany, 1977.

39. Durst, F., Melling, A. and Whitelaw, J. H., *Principles and Practice of Laser Doppler Anemometry*, Academic Press, New York, 1976.

40. Rudd, M. J., "A New Theoretical Method for the Laser Dopplermeter", *J. Phys. E:Sci. Instrum.*, 2, pp 55-59, 1969.

41. Tchen, C. M., "Mean Value and Correlation Problems Connected with the Motion of Small Particles Suspended in a Turbulent Fluid", *PHD Thesis*, Delft, 1947.

42. Dring, R. P., "Sizing Criteria for Laser Anemometry Particles", *J. Fluids Engineering*, 104, pp 15-17, 1982.

43. Patankar, S. V., *Numerical Heat Transfer and Fluid Mechanics*, Hemispherical Publishing Co., New York, 1980.

44. Klein, D. B. and Catton, I., "Analysis of Heat Pipe Vapor Dynamics", *Report INSPI-IR-UCLA-87-01, UCLA, Sept. 1987.*

45. Fletcher, C. A. J., *Computational Galerkin Methods, Spriger-Verlog, New York, 1984.*

46. Schrage, R. W., *A Theoretical Study of Interphase Mass Transfer, Columbia Univercity Press, New York, 1953.*

47. Callen, H. B., *Thermodynamics, John Wiley, New York, 1960.*